Cell Systems

Localization of signaling receptors maximizes cellular information acquisition in spatially structured natural environments

Graphical abstract

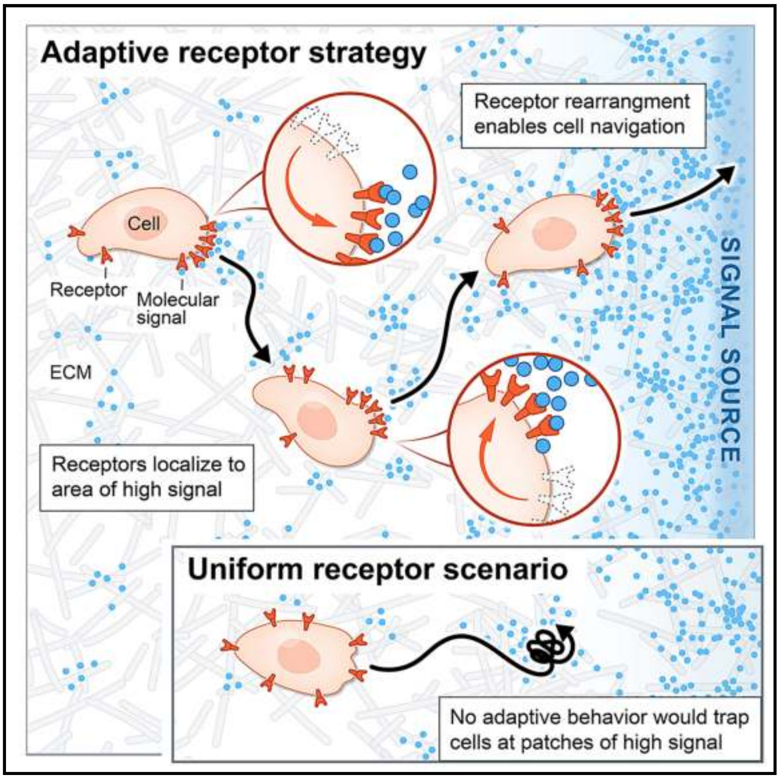

Authors

Zitong Jerry Wang, Matt Thomson

Correspondence

zwang2@caltech.edu (Z.J.W.),
mthomson@caltech.edu (M.T.)

In brief

Cells in natural environments, such as tissue or soil, sense and respond to extracellular ligands with intricately structured and non-monotonic spatial distributions. Using theory and computation, Wang et al. show that cell sensing and navigation can be optimized by adapting the spatial organization of signaling receptors to the spatial structure of the environment. The optimal receptor organization strategy, when implemented using simple feedback, boosts cell navigation efficiency in simulated tissue by 30-fold.

Highlights

- A mathematical framework computes sensing strategies in natural environments
- Receptor localization observed in cells optimizes sensing in tissue and soil
- A simple feedback circuit implements the optimal localization strategy
- Circuit boosts cell navigation efficiency by 30-fold in simulated tissue environment

Wang & Thomson, 2022, Cell Systems *13*, 530–546
July 20, 2022
https://doi.org/10.1016/j.cels.2022.05.004

CellPress
OPEN ACCESS

Cell Systems

Article

Localization of signaling receptors maximizes cellular information acquisition in spatially structured natural environments

Zitong Jerry Wang[1],* and **Matt Thomson**[1,2],*
[1]Division of Biology and Biological Engineering, California Institute of Technology, Pasadena, CA 91125, USA
[2]Lead contact
*Correspondence: zwang2@caltech.edu (Z.J.W.), mthomson@caltech.edu (M.T.)
https://doi.org/10.1016/j.cels.2022.05.004

SUMMARY

Cells in natural environments, such as tissue or soil, sense and respond to extracellular ligands with intricately structured and non-monotonic spatial distributions, sculpted by processes such as fluid flow and substrate adhesion. In this work, we show that spatial sensing and navigation can be optimized by adapting the spatial organization of signaling pathways to the spatial structure of the environment. We develop an information-theoretic framework for computing the optimal spatial organization of a sensing system for a given signaling environment. We find that receptor localization previously observed in cells maximizes information acquisition in simulated natural contexts, including tissue and soil. Specifically, information acquisition is maximized when receptors form localized patches at regions of maximal ligand concentration. Receptor localization extends naturally to produce a dynamic protocol for continuously redistributing signaling receptors, which when implemented using simple feedback, boosts cell navigation efficiency by 30-fold.

INTRODUCTION

Cells sense and respond in spatially structured environments, where signal distributions are determined by various chemical and physical processes such as substrate binding and fluid flow (Fowell and Kim, 2021). In tissue and soil, distributions of extracellular ligands can be spatially discontinuous, consisting of local ligand patches (de Anna et al., 2021; Hodge, 2006; Kennedy et al., 2006; Kicheva et al., 2007; Lim et al., 2015; Milde et al., 2008; Nunan et al., 2001; Raynaud and Nunan, 2014; Russo et al., 2016; Sarris et al., 2012; von Philipsborn et al., 2006; Weber et al., 2013; Yang et al., 2007). In tissue, diffusive signaling molecules are transported by interstitial fluid through a porous medium. These molecules are then captured by cells and a non-uniform network of extracellular matrix (ECM) fibers, taking on a stable and highly reticulated distribution (Kennedy et al., 2006; Kicheva et al., 2007; Russo et al., 2016; Sarris et al., 2012; Weber et al., 2013; Yang et al., 2007). For example, ECM-bound chemokine (CCL21) gradients extending from lymphatic vessels take on stable spatial structures, characterized by regions of high ligand concentration separated by spatial discontinuities (Weber et al., 2013). Similar observations have been made for the distribution of other chemokines, axon guidance cues, and morphogens in tissues (Kennedy et al., 2006; Kicheva et al., 2007; Lim et al., 2015; Sarris et al., 2012). In soil, a heterogeneous pore network influences the spatial distribution of nutrients by dictating both the locations of nutrient sources as well as where nutrients likely accumulate (de Anna et al., 2021; Hodge, 2006; Nunan et al., 2001; Raynaud and Nunan, 2014). Free-living cells detect chemical cues released by patchy distributions of microorganisms, where molecules are moved via fluid flow and diffusion (Hodge, 2006; Raynaud and Nunan, 2014). Cells in these and other natural environments experience surface ligand profiles with varying concentration peaks, non-continuity, and large dynamic range (Dlamini et al., 2020; Kennedy et al., 2006), differing strongly from smoothly varying, purely diffusive environments.

Modern signal processing theory shows that sensing strategies must adapt to the statistics of the input signals, suggesting that spatial sensing in cells should be adapted to the spatial structure of signaling molecules in the cells' native environments (Candès and Wakin, 2008). For example, when designing electronic sensor networks sensing spatial phenomena, adapting sensor placement to the spatial statistic of the signal can improve information acquisition (Krause et al., 2008). Furthermore, spatial navigation where sensing plays a key role may also benefit from sensor placement adaptation, as suggested by work from both robot and insect navigation (Huston et al., 2015; Iida and Nurzaman, 2016). For example, when navigating turbulent plumes, locusts actively move their antennae to odorant locations to acquire more information on source location (Huston et al., 2015). In the context of cell navigation, interstitial gradients can potentially trap cells in local concentration peaks (Weber et al., 2013). Cells that can adapt sensing to the patchy structure of the gradient may overcome local traps.

Traditional approaches to studying cell sensing often use highly simplified environmental models, where signals are either uniform or monotonic, neglecting the complex spatial structure in natural cell environments (Berg and Purcell, 1977; Endres and Wingreen, 2008; Hu et al., 2010; Mugler et al., 2016). Classic work, beginning with the seminal paper by Berg and Purcell (1977), studied cell sensing within homogeneous environments (Berg and Purcell, 1977). This and subsequent works were extended to study the detection of spatially varying concentrations, where monotonic gradients remain the canonical environmental model (Endres and Wingreen, 2008; Hu et al., 2010; Mugler et al., 2016). Recent work has started to address spatial complexity (Chou et al., 2011), but much work remains to understand how cell sensing strategies are affected by natural signal distributions, particularly spatially correlated fluctuations. Such complexity can pose challenges to cell engineering applications, such as CAR-T cell responses to tumor microenvironments (Martinez and Moon, 2019). Fundamentally, it is not clear what sense and response strategies are well adapted to operate in environments where signals take on complex spatial structures.

Interestingly, empirical observations suggest that cells might modulate the placement of their surface receptors to exploit the spatial structure of ligand distribution in its environment (Belema-Bedada et al., 2008; Bouzigues et al., 2007; Mossman et al., 2005; Nieto et al., 1997; Pignata et al., 2019; Shimonaka et al., 2003; van Buul et al., 2003; Yokosuka et al., 2005). For example, some axon guidance receptors, such as Robo1 and PlxnA1, can dynamically rearrange on the surface of growth cones (GCs) (Bouzigues et al., 2007; Pignata et al., 2019). In such cases, receptors constantly rearrange, adjusting local surface densities in response to changes in ligand distribution across the cell surface. Some chemokine receptors in lymphocytes, such as CXCR4 and CCR2, exhibit similar spatial dynamics (Nieto et al., 1997; Shimonaka et al., 2003; van Buul et al., 2003). Disrupting dynamic rearrangement of CCR2 on the surface of mesenchymal stem cells, without changing its expression level, severely inhibits targeted cell migration to damaged muscle tissues (Belema-Bedada et al., 2008). However, other chemotactic receptors (such as C5aR on the surface of neutrophils) remain uniform even when their ligands are distributed non-uniformly (Vicente-Manzanares and Sánchez-Madrid, 2004). In addition, during antigen recognition, T cell receptors (TCRs) take on different placements, ranging from uniform to highly polarized, depending on the density of antigen molecules on the surface of the opposing cell (Majzner et al., 2020). Thus, across a diverse range of cell surface receptors, we see different, even contradictory rearrangement behavior in response to changes in environmental structure. It remains unclear whether dynamic receptor rearrangement has an overarching biological function across disparate biological contexts.

Inspired by previous works that applied information maximization principles to understand the design of biological systems for signal processing (Cheong et al., 2011; Dubuis et al., 2013; Monti et al., 2018; Petkova et al., 2019; Sokolowski and Tkačik, 2015; Tkačik et al., 2008, 2009; Tkačik and Gregor, 2021), we formulate an information-theoretic framework and show that spatial localization of cell surface receptors is an effective spatial sensing strategy in natural cell environments, but relatively inconsequential in purely diffusive environments. Our framework allows us to solve for receptor placements that maximize information acquisition in natural environments, while generating such environments using existing computational models of tissue and soil microenvironments. We find that anisotropic receptor dynamics previously observed in cells are nearly optimal. Specifically, information acquisition is maximized when receptors form localized patches at regions of maximal ligand concentration. Optimizing receptor placement offers a substantial gain in information acquisition over uniformly distributed receptors, but only in natural cell habitats, leading to an average of ~ 1 bit of information gain in tissues and soils but only ~ 0.01 bits in purely diffusive gradients. The optimal strategy maximizes information by taking advantage of patchy ligand distribution in natural environments, reallocating sensing resources to a small but high signal region on the cell surface, while explicitly "ignoring" ligand information at low signal regions.

Our framework extends naturally to produce a dynamic protocol for continuously redistributing receptors across the cell surface in response to a dynamic environment. We show through simulation that a simple feedback circuit implements this protocol within a cell, redistributing receptors in a signal-dependent manner, and in doing so improving cell navigation. Compared with cells with uniform receptor placement, cells with this circuit achieve more than 30-fold improvement in their ability to localize to the peak of simulated interstitial gradients. Furthermore, our model accurately predicts spatial distributions of membrane receptors observed experimentally (Bouzigues et al., 2007; Nieto et al., 1997; Pignata et al., 2019; Shimonaka et al., 2003; van Buul et al., 2003). Our framework easily extends to study how spatial organization of many different cellular components, beyond receptor placement, affects information processing (see discussion). Taken together, our model serves as a useful conceptual framework for understanding the role of spatial organization of signal transduction pathways in cell sensing and provides a sensing strategy that is both effective in natural cell environments and amenable to cell engineering.

RESULTS

An optimal coding framework allows the computation of optimal receptor placement given spatial signal statistics

We are interested in optimal strategies for a task we refer to as spatial sensing. Spatial sensing is an inference task where a cell infers external profiles of varying ligand level across its surface from an internal profile of varying receptor activity across its membrane. This task is a useful model since optimizing performance on this task should improve the cell's ability to infer diverse environmental features.

We developed a theoretical framework to study whether manipulating the placement of cell surface receptors can improve spatial sensing performance. Optimizing spatial sensing by tuning receptor placement is analogous to optimizing distributed electronic sensor network by adjusting the location of sensors, which has been extensively studied in signal processing (Krause et al., 2008). In the optimization of distributed sensor networks monitoring spatial phenomena (Figure 1A), it is well-known that adjusting the placement of a limited number of

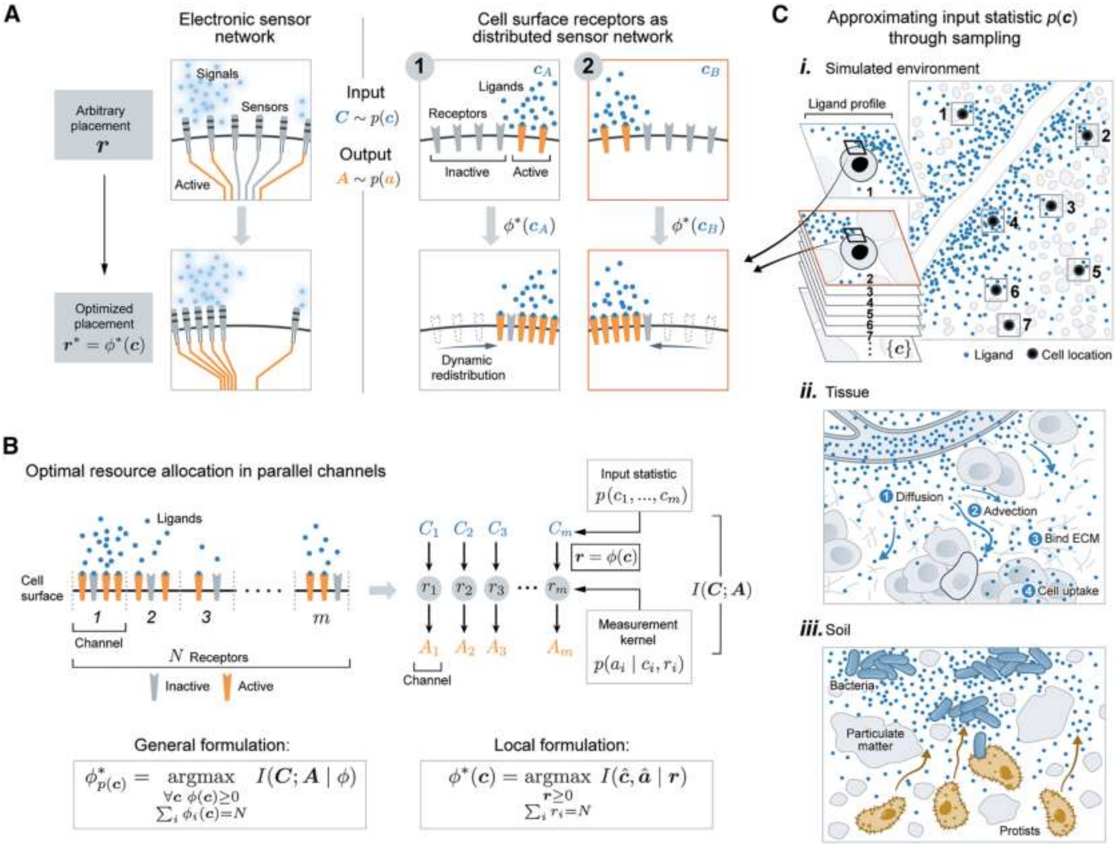

Figure 1. Adapting receptor placements to signal (input) statistic of natural cell environments

(A) (Left) Tuning sensor placement can boost the performance of electronic sensor network. (Right) Cell surface receptors also function as a sensor network, taking as inputs ligand profiles $\boldsymbol{C}$ across the cell surface and producing as outputs a profile of receptor activity $\boldsymbol{A}$ across the cell membrane. The optimal receptor placement strategy $\varphi^* : \boldsymbol{c} \rightarrow \boldsymbol{r}$ maps each ligand profile to a receptor placement, such that the mutual information $I(\boldsymbol{C};\boldsymbol{A})$ is maximized.

(B) The problem of optimal receptor placement formulated as a resource allocation problem over parallel, noisy communication channels. The ith channel represents the ith region of the cell membrane, with input C_i, output A_i and receptor number r_i. The input statistic $p(\boldsymbol{c})$ depends on the environment, and the measurement kernel $p(a_i|c_i, r_i)$ is modeled as a Poisson counting process. The general formulation of the optimal strategy φ^* allocates N receptors to m channels for each ligand profile $\boldsymbol{c}$, such that $I(\boldsymbol{C}, \boldsymbol{A})$ is maximized (Equation 2). The local formulation selects the receptor placement $\varphi^*(\boldsymbol{c})$ that maximizes $I(\widehat{\boldsymbol{c}}, \widehat{\boldsymbol{a}})$, where $\widehat{\boldsymbol{c}}$ is a Poisson random vector with mean equal to $\boldsymbol{c}$ (Equation 4).

(C) (Ci) Approximating input statistic by simulating natural environments and sampling ligand profiles $\{\boldsymbol{c}\}$ by tiling cells uniformly across the environment; (Cii) modeling ligand distribution in tissue microenvironment by incorporating diffusion, advection, ECM binding, degradation, and cell uptakes. (Ciii) Modeling ligand distribution in soil microenvironment by generating bacteria distributed in spatial patches, releasing diffusive ligands.

sensors can boost sensing performance, where the optimal placement strategy is dictated by the statistics of the input signals (Caselton and Zidek, 1984; Krause et al., 2008). The collection of a limited number of receptors on the cell surface also functions as a distributed sensor network, sensing a spatial profile of varying ligand concentration (Figure 1A). Therefore, we hypothesized that receptor placement can be tuned to improve spatial sensing and that the optimal strategy depends on the statistics of ligand profiles that cells typically encounter. Unlike traditional works in sensor optimization which focuses on finding a single "best" placement (Krause et al., 2008), cells can rearrange their receptors within a matter of minutes (Bouzigues et al., 2007), leading to a potentially much richer class of strategies.

Before presenting the general optimization problem, we set up the mathematical framework through the lens of information theory. Consider a two-dimensional (2D) cell with a 1D membrane surface. By discretizing the membrane into m equally sized regions, we modeled the membrane receptor system as m parallel communication channels (Figure 1B). The input to these m channels is $\boldsymbol{C} = (C_1, \ldots, C_m)$, where C_i is a random variable representing the amount of ligands at the ith membrane region. The receptor profile $\boldsymbol{r} = (r_1, .., r_m)$ denotes the amount of receptors allocated to each membrane region. The output $\boldsymbol{A} = (A_1, \ldots, A_m)$ is the amount of active receptors across the membrane, which depends on $\boldsymbol{c}$ and $\boldsymbol{r}$ through $p(\boldsymbol{A} = \boldsymbol{a}|\boldsymbol{c},\boldsymbol{r})$, the measurement kernel. Consider a placement strategy $\varphi : \boldsymbol{c} \rightarrow \boldsymbol{r}$, mapping a ligand profile to a receptor placement (Figure 1B). For a fixed number of receptors N, we are interested in the choice of φ that maximizes the mutual information $I(\boldsymbol{C};\boldsymbol{A})$ between the channels' inputs $\boldsymbol{C}$ and outputs $\boldsymbol{A}$, defined as:

$$I(\boldsymbol{C};\boldsymbol{A}) = \sum_{\boldsymbol{c} \in \boldsymbol{C}} \sum_{\boldsymbol{a} \in \boldsymbol{A}} p(\boldsymbol{c}, \boldsymbol{a}) \log \frac{p(\boldsymbol{c}, \boldsymbol{a})}{p(\boldsymbol{c}) p(\boldsymbol{a})}. \qquad \text{(Equation 1)}$$

The mutual information quantifies the "amount of information" obtained about $\boldsymbol{C}$ by observing $\boldsymbol{A}$. It is minimized when $\boldsymbol{C}$ and $\boldsymbol{A}$ are independent and maximized when one is a deterministic function of the other. All logs are taken in base 2, so information is report in units of bits. Importantly, note the choice of m (membrane bins) sets an upper bound on the mutual information and hence sets the scale for all information value reported in this paper (STAR Methods). Mathematically, the optimal strategy φ^* can be written as

$$\varphi^*_{p(\boldsymbol{c})} = \underset{\substack{\forall \boldsymbol{c}\ \varphi(\boldsymbol{c}) \geq 0 \\ \sum_i \varphi_i(\boldsymbol{c}) = N}}{\operatorname{argmax}} I(\boldsymbol{C};\boldsymbol{A}|\varphi, p(\boldsymbol{c})), \qquad \text{(Equation 2)}$$

where N is the total number of receptors which is taken to be a constant. Note the mutual information converges toward its upper bound as N increases (Figure S1A). The mutual information is agnostic to the decoding process in that it does not assume any details about downstream signaling, nor the exact environmental features a cell may try to decode, expanding the scope of our results.

To solve for φ^*, we needed to specify both a measurement kernel $p(\boldsymbol{a}|\boldsymbol{c},\boldsymbol{r})$ and an input statistic $p(\boldsymbol{c})$. We modeled $p(\boldsymbol{a}|\boldsymbol{c},\boldsymbol{r})$ assuming that each receptor binds ligands locally and activates independently. Furthermore, each local sensing process is modeled as a Poisson counting process. These assumptions yield the following measurement kernel:

$$p(\boldsymbol{A} = \boldsymbol{a}|\boldsymbol{C} = \boldsymbol{c},\ \boldsymbol{r}) = \prod_{i=1}^{m} \frac{\mu_i^{a_i}}{a_i!} e^{-\mu_i}, \qquad \text{(Equation 3)}$$

where $\mu_i = r_i\left(\frac{c_i}{c_i + K_d} + \alpha \frac{K_d}{c_i + K_d}\right)$ is the average number of active receptors at the ith membrane region. K_d is the equilibrium dissociation constant and α accounts for constitutive activity of receptors observed in cells, including many GPCRs, which we take to be small ($\alpha \ll 1$) (Seifert and Wenzel-Seifert, 2002; Slack and Hall, 2012). The bracket term represents the probability of receptor activation, and the fractional term $\frac{K_d}{c_i + K_d}$ ensures it is always less than 1 (Buchwald, 2019).

Next, we specify the input statistic $p(\boldsymbol{c})$ for three classes of environments: soil, tissue, and monotonic gradient. For each class of environment, we constructed $p(\boldsymbol{c})$ empirically, by computationally generating a ligand concentration field as the steady-state solution of a partial-differential equation (PDE), and sampling ligand profiles ($\{\boldsymbol{c}\}$) from them by evaluating the PDE solution around cells placed at different spatial locations (Figure 1Ci) (STAR Methods). Putting the empirical measure on the samples $\{\boldsymbol{c}\}$ approximates the true distribution of $\boldsymbol{C}$. For soil, we follow mathematical models from (Melke et al., 2010) and (Raynaud and Nunan, 2014), modeling diffusive ligands released from a group of soil bacteria whose spatial distribution agrees with the statistical properties of real soil colonies (Figures 1Ciii and 2A). For tissue, we adopted models from Milde et al. (2008) and Rejniak et al. (2013), where they modeled diffusive ligands released from a localized source, perturbed by *in vivo* processes such as interstitial fluid flow and heterogeneous ECM binding, leading to an immobilized interstitial gradient (Figures 1Cii and 2B). We also considered a monotonic gradient (Figure 2B) as an exponential fit to the simulated interstitial gradient. Fitting ensures any difference between the two environments are due to differences in local structures, not global features such as gradient decay length or average concentration. It is important to note that the overall framework can accommodate any choice of $p(\boldsymbol{c})$ and $p(\boldsymbol{a}|\boldsymbol{c})$ beyond what we have considered.

We are interested in the functional relationship between ligand profiles $\{\boldsymbol{c}\}$ and their optimal receptor placements $\{\varphi^*(\boldsymbol{c})\}$. To this end, we computed the optimal receptor placement for each sampled profile $\boldsymbol{c}$ individually, reducing the general formulation to a local formulation. Given ligand profile $\boldsymbol{c}$, random vector $\widehat{\boldsymbol{c}}$ represents local fluctuations of $\boldsymbol{c}$ due to stochasticity of reaction-diffusion events. In the case of unimolecular reaction-diffusion processes, it can be shown that $\widehat{\boldsymbol{c}}$ is a Poisson vector with mean equal to $\boldsymbol{c}$, solution of the PDE. Therefore, we can solve for $\varphi^*(\boldsymbol{c})$ locally by maximizing the mutual information between $\widehat{\boldsymbol{c}}$ and the resulting output $\widehat{\boldsymbol{a}}$:

$$\varphi^*(\boldsymbol{c}) = \underset{\substack{\boldsymbol{r} \geq 0 \\ \sum_i r_i = N}}{\operatorname{argmax}} I(\widehat{\boldsymbol{c}}, \widehat{\boldsymbol{a}}|\boldsymbol{r}), \qquad \text{(Equation 4)}$$

where $p(\widehat{\boldsymbol{a}}) = \sum_{\boldsymbol{c}} p(\widehat{\boldsymbol{a}}|\widehat{\boldsymbol{c}} = \boldsymbol{c})p(\widehat{\boldsymbol{c}} = \boldsymbol{c})$. The main difference between the general formulation of Equation 2 and local formulation of Equation 4 is their dependence on the input statistic $p(\boldsymbol{c})$. In the general formulation, the strategy $\varphi^*_{p(\boldsymbol{c})}$ is explicitly parametrized by $p(\boldsymbol{c})$. In the local formulation, φ^* is independent of the choice of $p(\boldsymbol{c})$. However, differences in $p(\boldsymbol{c})$ between environments will still crucially affect the set of optimal receptor profiles that cells will actually adopt because changing $p(\boldsymbol{c})$ changes the region of the domain of φ^* that is most relevant, thus changing the optimal receptor profiles that are actually used in different environments. For example, suppose environment A and B have input statistic p_A and p_B, and any ligand profile observed in A is not observed in B, and vice versa. Although φ^* is the same between A and B, this function is being evaluated on entirely different ligand profiles in A compared to B, so that receptor profiles observed in the two environment will likely be very different, in ways dictated by differences between their input statistic p_A and p_B. As a result, the statistical structure over the space of ligand profiles plays an important role in determining which receptor placement is effective, even when the placements are computed locally for each ligand profile.

Receptor localization yields optimal spatial sensing in natural environments

Optimal strategies of receptor placement are similar for soil and tissue environment, where receptors are highly localized within membrane positions experiencing high ligand concentrations. Figure 2Bi shows three examples of optimal receptor placements $\varphi^*(\boldsymbol{c})$ (colored) with the corresponding ligand profile $\boldsymbol{c}$, one from each class of environments shown in Figure 2A. In all three cases, the peak of each optimal receptor profile is oriented toward the position of highest ligand concentration. Compared with monotonic gradient, receptor profiles optimized for the ligand profiles sampled from tissue and soil are highly localized, with around 80% of receptors found within 10% of the membrane. In general, the optimal strategy consistently allocates more receptors to regions of higher ligand concentration, but

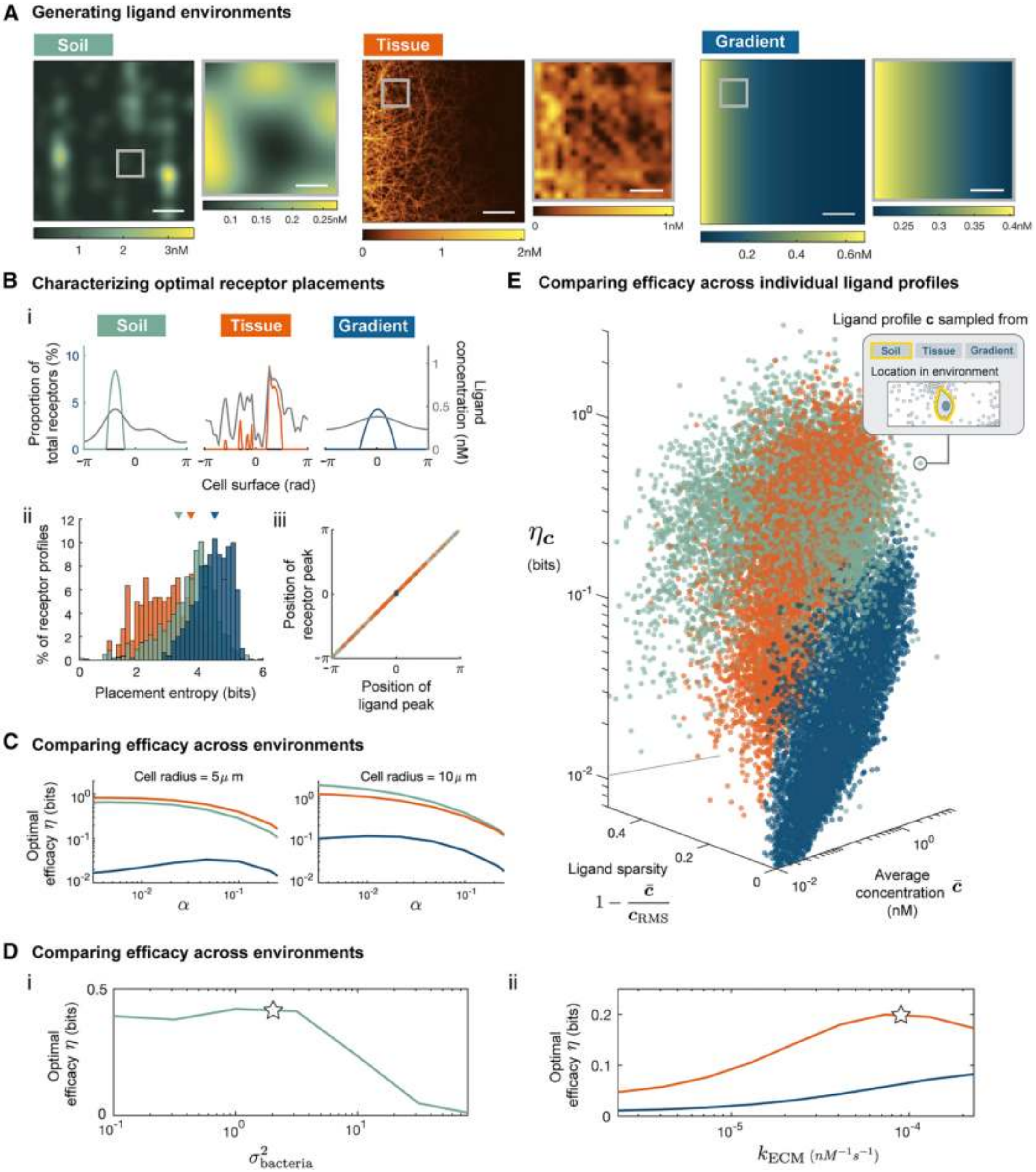

Figure 2. Receptor localization optimizes information acquisition in natural environments

(A) Computationally generated ligand concentration fields using PDE models of soil (left), tissue (interstitium) (middle), and simple exponential gradient (right, fitted to tissue with correlation index $R^2 = 0.98$); for each environment, zoomed-in field of view (FOV) scalebars are 10 μm, larger FOV scalebars are 50 μm, see Table S1 for environment simulation parameters.

(B) (Bi) Example of optimal receptor profile $\varphi^*(\boldsymbol{c})$ (colored) and the corresponding ligand profile $\boldsymbol{c}$ (gray); (Bii) entropy for each optimal receptor placements in $\{\varphi^*(\boldsymbol{c})\}$ colored by environment, colored triangles indicate the entropy of three receptor placements shown in (Bi); (Biii) scatter plot where each dot corresponds to an optimal placement $\varphi^*(\boldsymbol{c})$, y axis is membrane position with the most receptor, x axis is membrane position with most ligand in $\boldsymbol{c}$.

(C) Optimal efficacy η colored by environments, computed with ligand profiles $\{\boldsymbol{c}\}$ sampled using cells of different radius, for receptors of different constitutive activity α; see Figure S1B for result with different bin number m.

(D) (Di) Efficacy for soils environment simulated using different values of $\sigma^2_{\text{bacteria}}$, (Dii) efficacy for tissue environment simulated using different values of k_{ECM}, and for exponential gradients fitted to each tissue (gradient). Stars correspond to parameter values used to generate (A)–(C) and (E).

(E) Scatterplot where each dot corresponds to a single pair of $\boldsymbol{c}$ and $\varphi^*(\boldsymbol{c})$, where $\boldsymbol{c}$ is sampled from environments as illustrated in Figure 1Ci; $\eta_{\boldsymbol{c}}$ is defined in Equation 10. Across all panels, N = 1,000, K_d = 40 nm , $\alpha = 0.1$, m = 100 (see Figures 7B and S4 for η with other parameters).

in a highly nonlinear manner. Figure 2Biii shows, across all sampled ligand profiles $\{\boldsymbol{c}\}$, the peak of receptor profiles always align with the peak of ligand profiles. However, instead of allocating receptors proportional to ligand level, receptors tend to be highly localized to a few membrane positions with the highest ligand concentrations.

Indeed, Figure 2Bii shows that optimal receptor profiles tend to have low entropy. The entropy of receptor profile $\boldsymbol{r}$, defined as $H(\boldsymbol{r}) = -\sum_i \frac{r_i}{N}\log\left(\frac{r_i}{N}\right)$, can be used as a measure of localization. Note the maximal value of this entropy measure is limited by the number of membrane bins m. Low entropy corresponds to receptor profiles where most receptors are concentrated to a few membrane positions, forming localized patches. Such high degree of localization is partly explained by low receptor numbers. When receptors are limited, information gain per receptor within each membrane channel is approximately independent of receptor number (STAR Methods). Thus, the optimal solution allocates all receptors to the channel with the highest information content (Figure S2). In addition, receptors are more localized for sensing in soil and tissue because locally, they exhibit greater spatial variations in ligand concentration compared with simple gradients (Figure 2A; STAR Methods). Absolute ligand concentration also influences the optimal strategy, which we take to be dilute in agreement with empirical measurements (Clark et al., 2015; Wang et al., 2008). In saturating environments, the optimal solution completely switches, allocating most receptors to regions of lowest ligand concentrations (STAR Methods; Figure S3). In summary, the optimal placement strategy φ^* in the environments studied can be approximated by a simple scheme, where receptors localize to form patches at positions of high ligand concentration.

Optimally placed receptors drastically improve information acquisition relative to uniform receptors, especially in soil and tissue environments. To make this statement precise, we quantified the efficacy of a receptor placement strategy $\varphi : \boldsymbol{c} \rightarrow \boldsymbol{r}$ with respect to a set of ligand profiles $\{\boldsymbol{c}\}$. First, we denote by I_φ the average amount of information acquired by cells adopting the placement strategy φ:

$$I_\varphi = \langle I(\widehat{\boldsymbol{c}};\widehat{\boldsymbol{a}}|\varphi)\rangle_{\boldsymbol{c}} \qquad \text{(Equation 5)}$$

where $\langle \cdot \rangle_{\boldsymbol{c}}$ denotes averaging across the set of sample ligand profiles $\{\boldsymbol{c}\}$, and recall $\widehat{\boldsymbol{c}}$ is a Poisson-distributed random vector with mean $\boldsymbol{c}$. In particular, we are interested in information acquisition using the uniform strategy φ^u (uniformly distributed receptors) and the optimal strategy φ^*:

$$I_{\text{unif}} := I_{\varphi^u},\ I_{\text{opt}} := I_{\varphi^*}. \qquad \text{(Equation 6)}$$

The efficacy of a placement strategy φ is the change in average information cells acquire by adopting the strategy φ compared with the uniform strategy:

$$\eta(\varphi) = I_\varphi - I_{\text{unif}}. \qquad \text{(Equation 7)}$$

In particular, we are interested in the optimal efficacy:

$$\eta(\varphi^*) = I_{\text{opt}} - I_{\text{unif}}, \qquad \text{(Equation 8)}$$

which we will refer to simply as η when the dependency is clear from context. For a particular $\eta(\varphi^*)$, the set of ligand profiles $\{\boldsymbol{c}\}$ referred to in its definition is always the same set that φ^* is optimized for. The larger η is, the more beneficial it is for cells to place receptors optimally rather than uniformly. We found that η is an order of magnitude larger for soil and tissue environment compared with a simple gradient (Figure 2C). This difference persists across cells of different size and across a wide range of receptor parameter values (Figures 2C, 7B, S4, and S5A). In other words, placing receptors optimally rather than uniformly benefits cells in complex, natural environments substantially more than cells in simple, monotonic gradients. Note that differences between tissue and monotonic gradient are due to differences in local spatial structure, not global features such as gradient decay length or global average concentration, as both parameters were made to be identical between the two environments. Lastly, although the mutual information is an exponential measure, so an improvement by one bit has different meaning depending on the baseline I_{unif}, this fact does not hinder interpretation of η as I_{unif} is similar between the three environments considered (Figure S4A).

In addition to the large difference in optimal efficacy (η) between natural environments and simple gradients, Figure S4 shows similar differences exist when comparing other metrics assessing the benefit of optimizing receptor placement, such as the relative information gain ($(I_{\text{opt}} - I_{\text{unif}})/I_{\text{unif}}$) and the absolute increase in the number of distinguishable input signals ($2^{I_{\text{opt}}} - 2^{I_{\text{unif}}}$). For example, optimizing receptor placement increases the number of distinguishable input states by 40 in tissue, while optimizing the same receptors in the (fitted) gradient environment leads to an increase of 1 state (Figure S4A). Note that in the limit of strong constitutive receptor activity, all placement strategies become equivalent to uniformly distributed receptors. Since receptor activation in the absence of ligands reduces statistical dependence between ligand level and receptor activity, the average information acquisition I_φ for any strategy φ converges to zero for large α, driving information gain compared with the uniform strategy to zero (Figure S4A).

For both soil and tissue environment, the optimal efficacy η depends on a key parameter in their respective PDE model. We illustrate this dependence by adjusting the value of each respective parameter, sampling new ligand profiles $\{\boldsymbol{c}\}$, solving for optimal placements $\{\varphi^*(\boldsymbol{c})\}$, and computing η. Figure 2D shows how η changes as we adjust environmental parameters. In soil, η drops substantially as ligand sources (bacteria) become more aggregated (Figure 2Di), corresponding to an increase in the parameter $\sigma^2_{\text{bacteria}}$ of the random process (STAR Methods) used to model bacterial distribution (star corresponds to empirical value from Raynaud and Nunan [2014]). The decrease in η is intuitive since increasing the extent of aggregation of sources makes the environment appear more like a simple gradient generated from a single ligand source. In tissue, optimal efficacy dropped when most ligands were found in solution, instead of bound to the ECM (Figure 2Dii), corresponding to low ECM-binding rate (k_{ECM}). For reference, star indicates the empirical value of k_{ECM} for the chemokine CXCL13 (Yang et al., 2007). Compared with its fitted monotonic gradient, η is higher in the interstitial gradient for all ECM-binding rates (Figures 2Dii and S5B). In tissue, gradients made up of ECM-bound ligands are ubiquitous, suggesting that the optimization of receptor placement is highly relevant.

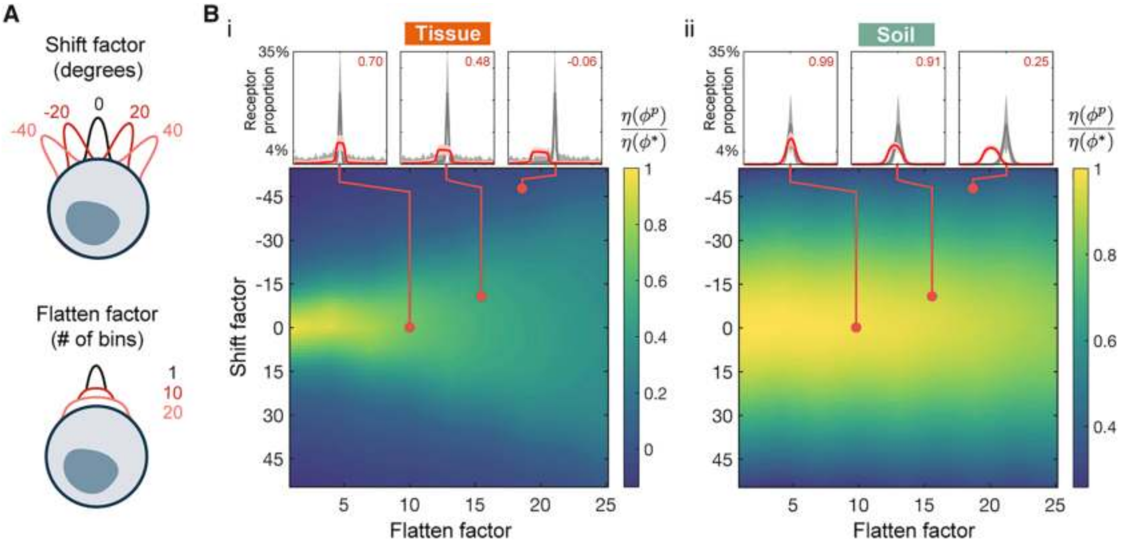

Figure 3. Optimal efficacy $\eta(\varphi^*)$ is robust to minor deviations in receptor placement away from the optimal form

(A) The effect of different degrees of shifting and flattening applied to a receptor profile (black curve).

(B) Colors of heatmap represent ratio of perturbed efficacy $\eta(\varphi^p)$ to optimal efficacy $\eta(\varphi^*)$ for different combinations of shifting and flattening, computed for ligand profiles $\{\boldsymbol{c}\}$ sampled from either soil or tissue; call-out boxes corresponds to different sets of perturbations, showing the average of the optimal $\{\varphi^*(\boldsymbol{c})\}$ (gray) and perturbed $\{\varphi^p(\boldsymbol{c})\}$ (red) receptor placements, after all ligand profile peaks were centered; red numbers indicate the value on heatmap; cell radius = 10 μm.

Optimal efficacy (η) is larger in soil and tissue because ligand profiles that cells encounter in such environments tend to be patchier, having most of the ligands concentrated in a small subset of membrane regions. We make this statement precise by quantifying patchiness of a ligand profile $\boldsymbol{c}$ using a measure of sparsity:

$$\text{sparsity}(\boldsymbol{c}) = 1 - \frac{\overline{\boldsymbol{c}}}{\boldsymbol{c}_{\text{RMS}}}, \qquad \text{(Equation 9)}$$

where the root-mean-square $\boldsymbol{c}_{\text{RMS}} = \sqrt{\frac{1}{m}\sum_i c_i^2}$ and $\overline{\boldsymbol{c}} = \frac{1}{m}\sum_i c_i$ is the average concentration of $\boldsymbol{c}$ across the membrane. A ligand profile with a sparsity of one has all ligands contained in a single membrane region, whereas a uniform distribution of ligands has a sparsity of zero. Next, we defined an efficacy measure $\eta_{\boldsymbol{c}}$ for each ligand profile $\boldsymbol{c}$:

$$\eta_{\boldsymbol{c}} = I(\widehat{\boldsymbol{c}};\widehat{\boldsymbol{a}}|\varphi^*) - I(\widehat{\boldsymbol{c}};\widehat{\boldsymbol{a}}|\varphi^u) = I_{\text{opt},c} - I_{\text{unif},c}, \qquad \text{(Equation 10)}$$

where again φ^u denotes uniform receptor distribution. Unlike η as defined in Equation 8, $\eta_{\boldsymbol{c}}$ does not involve the averaging across the entire set $\{\boldsymbol{c}\}$ through $\langle\,\cdot\,\rangle_{\boldsymbol{c}}$, it measures improvement in information gain for only a single ligand profile $\boldsymbol{c}$. The larger $\eta_{\boldsymbol{c}}$ is, the more useful the optimal placement is for sensing $\boldsymbol{c}$ compared with a uniform profile. Each dot in Figure 2E corresponds to a ligand profile sampled from an environment, as illustrated in Figure 1Ci. Figure 2E shows that (1) across a wide range of concentrations, sparser ligand profiles tend to induce higher efficacy $\eta_{\boldsymbol{c}}$ and (2) ligand profiles sampled from soil and tissue tend to be sparser compared with profiles from the corresponding monotonic gradient. Taken together, since signals cells encounter in natural environments tend to have sparse concentration profiles, cells can improve their spatial sensing performance by localizing receptors to regions of high ligand concentration.

In summary, the value of optimizing receptor placement as a sensing strategy depends strongly on the environmental structure. Patchy ligand distributions found in tissue and soil environments makes optimizing receptor placement a highly effective sensing strategy. Our result demonstrates that uncovering effective cell sensing strategies requires a careful consideration of the spatial structure of the cells' natural habitat.

Spatial sensing via the optimal strategy is robust to imprecise placements caused by biological constraints

Despite the optimal strategy φ^* being highly localized and precisely oriented, we found that neither features are necessary to achieve high efficacy. Given the stochastic nature of biochemical processes in cells, this robustness is crucial as it makes the strategy feasible in cells. Fortunately, receptors do not need to adopt φ^* precisely in order to obtain substantial information gain. To illustrate, we perturb the optimal placements and show that sensing efficacy persists when receptors partially align with ligand peak and localize weakly. For soil and tissue, we circularly shift and flatten (by applying a moving average) all optimal receptor profiles $\{\varphi^*(\boldsymbol{c})\}$ computed from sample ligand profiles to obtain $\{\varphi^p(\boldsymbol{c})\}$, the corresponding set of perturbed profiles. Different degrees of shifting and flattening represents different degrees of misalignment and weakened localization, respectively. Figure 3A shows results of different perturbations (colored) applied to a receptor profile (black). To assess the effect of these perturbations on sensing, we compute the efficacy $\eta(\varphi^p)$ of the perturbed profiles and compare it with the optimal efficacy $\eta(\varphi^*)$. The heatmap in Figure 3B shows the ratio of perturbed to optimal efficacy for various combinations of perturbations, across soil and tissue. Figure 3Bi shows two examples of perturbations (red dots) that drastically alter the receptor profile while still achieving high efficacy. The red and gray curve in the

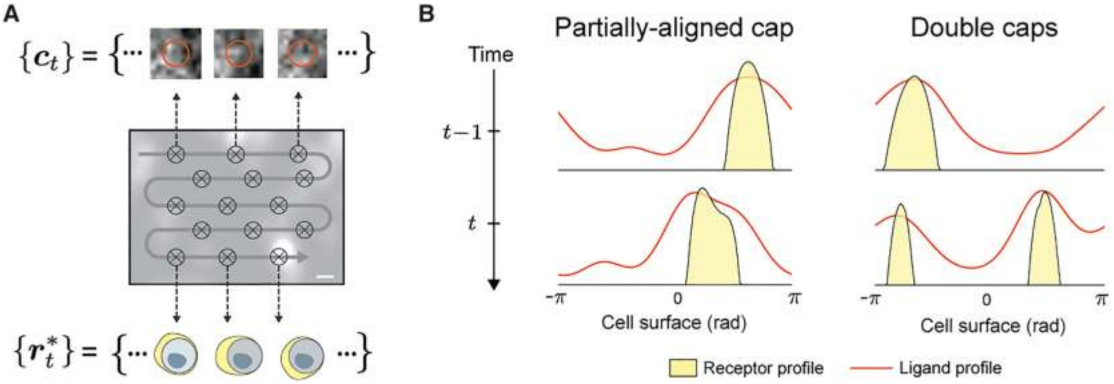

Figure 4. A dynamic receptor placement protocol based on maximizing rate of information gain

(A) Schematic showing a cell moving along a path (gray curve) sensing a sequence of ligand profiles $\{\boldsymbol{c}_t\}$ at points (crosses) along the path, using receptor placements $\{\boldsymbol{r}_t^*\}$ generated by the dynamic protocol.

(B) Accounting for transport cost, the optimal placement strategy is modified to localize receptors to an intermediate position between subsequent ligand peaks or form multiple receptor peaks.

call-out box represents what the "average" perturbed and optimal profiles look like, respectively. They are obtained by circularly shifting each profile in $\{\varphi^p(\boldsymbol{c})\}$ and $\{\varphi^*(\boldsymbol{c})\}$ so the peak of $\boldsymbol{c}$ is center, followed by averaging across the set of shifted profiles element-wise. Clearly, highly localized receptors ($>80\%$ of receptors found within 10% of membrane) are not necessary for effective sensing. In fact, compared with uniformly distributed receptors, a modest enrichment of receptors oriented toward the ligand peak (4-fold relative to uniform) already provides substantial information gain (Figure 3B). Importantly, enrichment of receptors (around the ligand peak) greater than 4- to 5-fold has been observed for different membrane receptors (van Buul et al., 2003; Wang et al., 2019), and in some cases, nearly all receptors redistribute toward the ligand peak (Bouzigues et al., 2007). Such robustness holds across different cell sizes and efficacy metric (Figure S6). In tissue, the heatmap of Figure 3Bi also shows that weakly localized receptors (large flatten factor) are more robust to misalignment (large shift factor). Altogether, the robustness results of Figure 3 suggest that biochemical implementations of receptor localization could improve sensing in natural or engineered cells, even in the presence of stochastic fluctuations in a biological circuit that induce imperfect localization. Moreover, the magnitude of receptor enrichment (around the ligand peak) previously observed in cells is sufficient to obtain substantial information gain (Bouzigues et al., 2007; van Buul et al., 2003; Wang et al., 2019).

Optimization framework extends naturally to produce a dynamic protocol for sensing time-varying ligand profiles

Our framework extends naturally to produce a dynamic protocol for rearranging receptors in response to dynamically changing ligand profiles. So far, we have viewed ligand profiles as static snapshots and considered instantaneous protocols for receptor placement. In reality, cells sense while actively exploring their environment, so that the ligand profile it experiences is changing in time, both due to intrinsic changes in the environment state as well as due to the motion of the cell. As the ligand profile $\boldsymbol{c}_t$ changes over time, we want the receptor profile $\boldsymbol{r}_t$ to change in an "efficient" manner to improve information acquisition (Figure 4A). Specifically, we obtain a dynamic protocol by extending our framework to account for both information acquisition and a "cost" for changing receptor location. We quantify the cost of moving receptors using the Wasserstein-1 distance $W_1(\boldsymbol{r}_A, \boldsymbol{r}_B)$, which is the minimum distance receptors must move across the cell surface to redistribute from profile $\boldsymbol{r}_A$ to $\boldsymbol{r}_B$ (STAR Methods). For a cell sensing a sequence of ligand profiles $\{\boldsymbol{c}_t\}_{t=1}^{T}$ over time, the optimal receptor placement $\boldsymbol{r}_t^*$ for $\boldsymbol{c}_t$ now depends additionally on $\boldsymbol{r}_{t-1}^*$, the optimal placement for the previous ligand profile:

$$\boldsymbol{r}_t^* = \underset{\substack{\boldsymbol{r} \geq 0 \\ \sum_i r_i = N}}{\operatorname{argmax}} \left(I(\hat{\boldsymbol{c}}_t; \hat{\boldsymbol{a}} | \boldsymbol{r}) - \gamma W_1\left(\boldsymbol{r}_{t-1}^*, \boldsymbol{r}\right) \right), \qquad \text{(Equation 11)}$$

where $p(\hat{\boldsymbol{a}}) = \sum_{\boldsymbol{c}} p(\hat{\boldsymbol{a}} | \hat{\boldsymbol{c}}_t) p(\hat{\boldsymbol{c}}_t)$, and $\gamma \geq 0$ represents the cost of moving one receptor per unit distance. The cost γ implicitly encodes a timescale for receptor redistribution. Smaller γ means less "cost" is associated with redistributing receptors; hence, the receptor profile becomes more dynamic. The exact relationship between γ and the speed of receptor redistribution depends on both receptor properties and the environment, see Figures S7A–S7D for an example of how receptor speed scales with γ. For $\gamma = 0$, the formulation of Equation 11 reduces to the original static formulation of Equation 4. This dynamic formulation admits a natural interpretation as maximizing information rate (information per receptor-distance moved) instead of absolute information gain. For $t = 1$, we define r_t^* according to the original formulation. Hence, we refer to the dynamic protocol of Equation 11 as the general optimal strategy since it encompasses φ^*. Figure 4B illustrates two salient features of this dynamic protocol. First (left), when the peak of the previous receptor profile $\boldsymbol{r}_{t-1}^*$ is near the peak of the current ligand profile $\boldsymbol{c}_t$, $\boldsymbol{r}_t^*$ is obtained by shifting receptors toward the current ligand peak but not aligning fully. Second (right), when the peak of the previous receptor profile is far from the current ligand peak, some receptors are moved to form an additional patch at the current ligand peak (Figure S7F shows how changing γ affects the

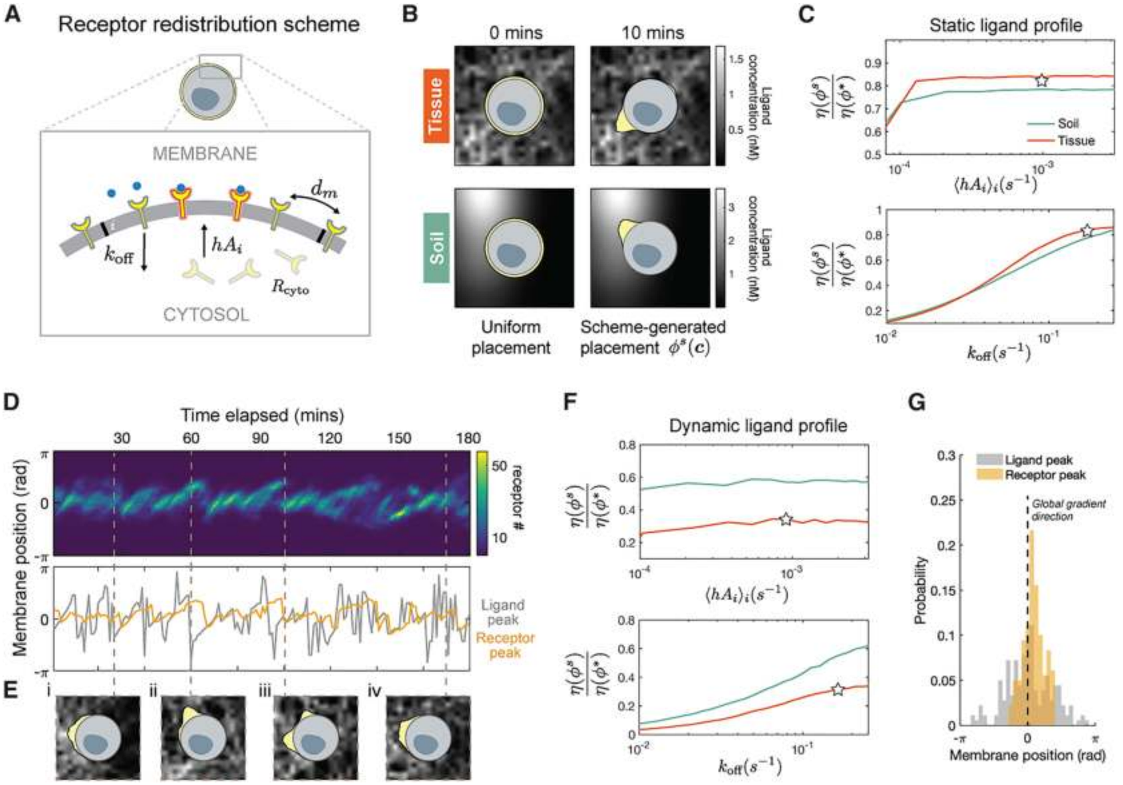

Figure 5. Positive feedback scheme redistributes receptors to achieve near-optimal sensing efficacy for both static and dynamic signals

(A) The cell is modeled as a one-dimensional membrane lattice with a well-mixed cytosol. Receptors are subject to three redistribution mechanisms: endocytosis (k_{off}), activity-dependent incorporation into membrane (hA_iR_{cyto}), membrane diffusion (d_m); the value of h sets the feedback strength between receptor activity and the rate with which receptors incorporate into the membrane; $h = 4 \times 10^{-3} s^{-1}$, $d_m = 1 \times 10^{-2} \mu m^2 s^{-1}$, $k_{\text{off}} = 1 \times 10^{-1} s^{-1}$ (Table S2).

(B) Receptor profiles (yellow) generated by simulating the feedback scheme for an initially uniform set of receptors, against a static ligand profile from tissue and soil, cell radius = 10 μm.

(C) Ratio of scheme efficacy $\eta(\varphi^s)$ to optimal efficacy $\eta(\varphi^*)$ for static signals $\{\boldsymbol{c}\}$ sampled from soil and tissue, stars indicate parameter values used for simulation in (B).

(D) (Top) Kymograph showing the entire temporal sequence of receptor profiles of a moving cell; (bottom) position of ligand peak aligned in time with position of receptor peak as generated by the feedback scheme.

(E) Snapshots of receptor profiles taken at select time points.

(F) Ratio of scheme efficacy $\eta(\varphi^s)$ to optimal efficacy $\eta(\varphi^*)$ for a sequence of signals $\{\boldsymbol{c}_t\}$ sampled by translating a cell through soil and tissue environment, stars indicate parameter values used for simulation in (D) and (E); cell radius = 10 μm (see Figures S9B and S9C for results with cell radius = 5 μm).

(G) Histogram showing the distribution of ligand peak (gray) and receptor peak (yellow) position on the membrane of the cell from (D), dashed black line indicates the direction of the global gradient with respect to membrane positions. See Table S2 for feedback scheme simulation parameters.

receptor behavior in Figure 4B). Receptor properties such as the strength of constitutive receptor activity (α) also affect receptor redistribution dynamics. For small α, receptors localize more readily to align with new ligand peaks because the mutual information term in Equation 11 becomes dominant over the cost of redistribution (Figure S7E). Although the formulation of Equation 11 is quite complex, this general optimal strategy can be achieved by a simple receptor feedback scheme.

Simple feedback scheme rearranges receptors to achieve near-optimal information acquisition

We show that a positive feedback scheme implements the general optimal strategy (Equation 11), dynamically redistributing receptors into localized poles to achieve near-optimal information acquisition. Asymmetric protein localization is a fundamental building block of many complex spatial behaviors in cells, involved in sensing, movement, growth, and division (Macara and Mili, 2008). Many natural localization circuits are well characterized down to molecular details (Hegemann et al., 2015; Zhu et al., 2020). Even synthetic networks have been experimentally constructed in yeast, capable of reliably organizing membrane-bound proteins into one or more localized poles (Chau et al., 2012). Such works demonstrate the feasibility of engineering new spatial organization systems in cells.

Using a PDE model of receptor dynamics, we show that simple, local interactions can redistribute receptors to achieve near-optimal information acquisition, for both static and dynamic signals. The core feedback architecture of our circuit design uses similar motifs as have been demonstrated in existing synthetic biology circuits (Chau et al., 2012). Figure 5A illustrates the three mechanisms (arrows) in our feedback scheme that affects receptor distribution (r), which can be expressed mathematically as

$$\frac{\partial r(x,t)}{\partial t} = D\nabla^2_{\mathrm{memb}} r - k_{\mathrm{off}}\, r + hAR_{\mathrm{cyto}}, \qquad \text{(Equation 12)}$$

where x denotes membrane position and t denotes time. The first term represents lateral diffusion of receptors on the membrane with uniform diffusivity D. The second term represents endocytosis of receptors with rate k_{off}. The last term represents incorporation of receptors to membrane position i from a homogeneous cytoplasmic pool (R_{cyto}) with rates hA_i, where h a proportionality constant and A_i is the local receptor activity (see STAR Methods for model details). Activity-dependent receptor recruitment provides the necessary feedback to enable ligand-dependent receptor redistribution. Recent works suggest that activity-dependent receptor recruitment can be achieved through biased docking and fusion of secretory vesicles that carry the receptors, to regions of high receptor activity (Hegemann et al., 2015; Kinoshita-Kawada et al., 2019; Wang et al., 2019). Budding yeasts Ste2 receptors achieve feedback using an interacting loop with intracellular polarity factor Cdc42 (Hegemann et al., 2015). Note that our feedback scheme is only meant to illustrate one possible implementation of the dynamic rearrangement protocol. Feasible alternatives such as activity-dependent endocytosis or microtubule-dependent receptor redistribution have also been proposed, providing a range of biochemical strategies for implementation of the optimal placement strategy (Bouzigues et al., 2007; Suchkov et al., 2010).

Given a fixed ligand profile $\boldsymbol{c}$, Figure 5B shows our feedback scheme can, within minutes, localize receptors (yellow) toward the position of maximum ligand concentration. The rapid localization is robust to changes in k_{off} and h across at least an order of magnitude (Figure S9A). We denote the steady-state receptor profile generated by our scheme in response to ligand profile $\boldsymbol{c}$ as $\varphi^s(\boldsymbol{c})$. As Figure 5B shows, scheme-generated profiles are far less localized than their optimal counterpart $\varphi^*(\boldsymbol{c})$. Despite this, Figure 5C shows scheme efficacy $\eta(\varphi^s)$ are close to that of the optimal value $\eta(\varphi^*)$. Recall $\eta(\varphi^*)$ measures the absolute increase in average information acquired using optimally placed instead of uniform receptors. Therefore, the scheme efficacy $\eta(\varphi^s)$ makes a similar comparison between scheme-driven and uniform receptors. In Figure 5C, we see scheme efficacy is robust to variations in both endocytosis (k_{off}) and average membrane incorporation rate ($\langle hA_i \rangle_i$), with other parameters fixed to empirical values (Marco et al., 2007). Stars represent parameters used to simulate profiles in Figure 5B.

Our feedback scheme (Equation 12) can continuously rearrange receptors in response to changes in ligand profile, exhibiting dynamics similar to the optimal dynamic protocol (Equation 11). Figures 5D and 5E shows a time-varying receptor profile, generated by the feedback scheme in a cell translating across the tissue environment. In this dynamic setting, the scheme can still induce asymmetric redistribution of receptors. Figure 5D (top) shows this dynamic asymmetry through a kymograph of a sequence of receptor profiles $\{\varphi^s(\boldsymbol{c}_t)\}$. As desired, snapshots along this sequence show receptors localize toward regions of high ligand concentration (Figure 5E). Receptor placements generated by our scheme exhibit features of the dynamic protocol shown in Figure 4B. First, as the ligand peak changes position slightly, the receptor peak gets shifted in the same direction after a delay. Figure 5D (bottom) illustrates this phenomena by aligning the time trace of both peak positions. Here, a shift in the ligand peak (gray) is often followed by a corresponding shift in receptor peak (yellow) after an appreciable delay; hence, there is only partial peak-to-peak alignment. Second, if the ligand peak changes position abruptly, a second receptor peak forms, oriented toward the new ligand peak. Figure 5Eiii illustrates this clearly by showing a new receptor peak forming precisely after a large shift in ligand peak position (Figure 5D). We assess the performance of our scheme by comparing scheme-generated placements $\{\varphi^s(\boldsymbol{c})\}$ and optimal placements $\{\varphi^*(\boldsymbol{c})\}$ corresponding to the same sequence of ligand profiles $\{\boldsymbol{c}_t\}$. Figure 5F shows that for cells moving in soil and tissue, scheme efficacy $\eta(\varphi^s)$ (star) is not far from the optimal value $\eta(\varphi^*)$. Furthermore, scheme efficacy is robust to variations in endocytosis (k_{off}) and average incorporation rate ($\langle hA_i \rangle_i$). Taken together, our feedback scheme organizes receptors to achieve near-optimal information acquisition, in both static and dynamic environments.

Our feedback scheme can align receptors with the global gradient direction, suggesting that this scheme may allow cells to escape local ligand concentration peaks within interstitial gradients. On the one hand, Figure 5G shows that the peak of ligand profiles (gray), as experienced by cells, do not always agree with the direction of the global gradient (dashed line)—a known feature of interstitial gradients (Weber et al., 2013). On the other hand, receptors organized by the feedback scheme (yellow) align very well with the global gradient direction. The effect of the feedback scheme comes from its ability to localize receptors and account for past receptor profiles. The latter allows the current receptor profile to carry memory of past ligand profiles that the cell has encountered, enabling a form of spatial averaging over ligand peaks. Alignment of receptors to the global gradient should provide substantial boost to cell navigation performance, especially in non-monotonic, interstitial gradients.

Feedback scheme enables cells to search quickly and localize precisely in simulated interstitial gradients

Cells using our feedback scheme effectively localizes to the ligand source of simulated interstitial gradients, while cells with uniform receptors become trapped away from the source by local concentration peaks. Immune cells can navigate toward the source of an interstitial gradient in a directed, efficient manner (Figure 6A; Weber et al., 2013). Efficient navigation can be difficult in complex tissue environments, partly due to the existence of local maxima away from the ligand source, potentially trapping cells on their way to the source (Figure 6B). By simulating cell navigation using standard models of directional decoding (STAR Methods), we found that cells with uniform receptors can indeed become trapped during navigation. Figure 6C demonstrates this behavior through the trajectories of individual cells with uniform receptors (blue), as they consistently become stuck within specific locations of the environment. On the other hand, using the same method of directional decoding, cells with scheme-driven receptors (orange) reliably reach the source in an efficient manner. Figure 6D illustrates this difference through a histogram of the time it took for a cell to reach the source, created by simulating cells starting at uniformly sampled locations 50 μm from the source, moving at a constant speed of 2 μm/min. Remarkably, for the circuit parameter values chosen, only 2% of cells (13/600)

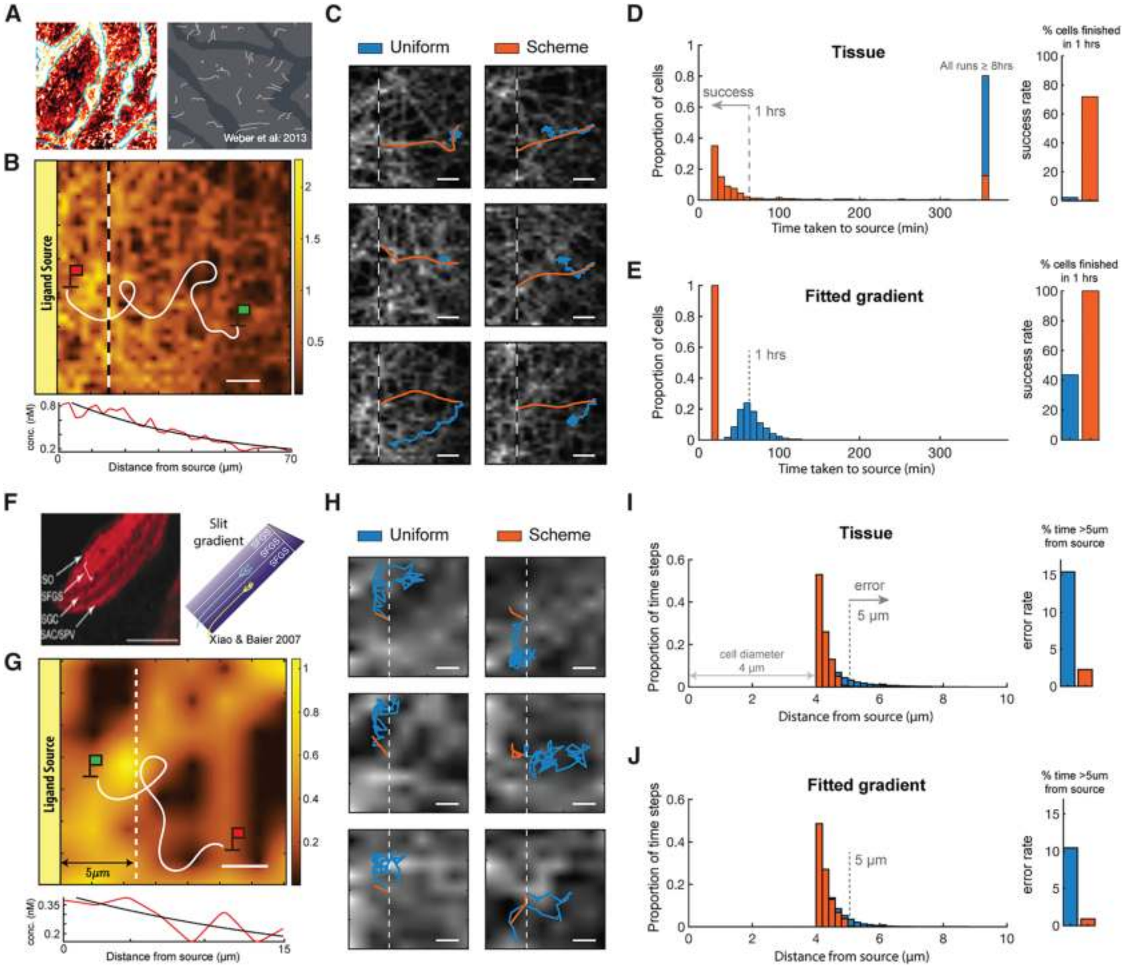

Figure 6. In simulated interstitial gradient, cells localize to source quickly and precisely when receptors are redistributed by the feedback scheme instead of uniformly distributed

(A) (Left) Interstitial CCL21 gradient, (right) white curves represent haptotactic trajectories of dendritic cells (Weber et al., 2013).

(B) (Top) Schematic of a navigation task where a cell (green flag) in a region of an interstitial gradient move toward the source (red flag) by sensing spatially distributed ligands and decoding source direction locally, the ligand field shown is a region of the tissue environment in Figure 2A obtained through PDE simulation (STAR Methods); (bottom) red curve shows the tissue ligand field averaged over the y direction, and black curve is the fitted exponential gradient, scale bars, 10 μm.

(C) Sample trajectories of repeated simulations of cells navigating with uniform receptors (blue) and with scheme-driven receptors (orange), all scale bars, 10 μm.

(D) (Left) Histogram of time taken to reach source across 600 cells at different starting positions of equal distance from source, note the rightmost bar includes all cells that did not reach the source after 8 h; (right) barplot showing percentage of runs completed in 1 h (success rate), see also Figure S10 for success rate across different simulation parameters.

(E) Same type of data as in (D) for cells navigating in an exponential gradient (fitted to the interstitial gradient used to generate (D)).

(F) Red stripes (left) represent growth cones moving within specific lamina along a slit gradient (right schematic), scale bars, 40 μm (Xiao and Baier, 2007).

(G) (Top) Schematic of a navigation task where a cell (green flag) senses its environment in order to remain close to source, solid white line represents cell trajectory, dotted white line demarcates a distance of 5 μm from ligand source (see Table S3 for tissue simulation parameters), an ellipse-shaped cell is used for this simulation to mimic navigating growth cone; (bottom) red curve shows the tissue ligand field averaged over the y direction, and black curve is the fitted exponential gradient, scale bars, 3 μm.

(H) Sample trajectories of repeated simulations of cells performing task with either uniform or scheme-driven receptors, all scale bars, 3 μm.

(I) (Left) Histogram of time spent by cell at various distance from the ligand source (measured from source to farthest point on cell, perpendicular to source edge) aggregated across 600 cells starting at different positions, moving for 2 h near the ligand source; (right) bar plot shows percentage of time the cell spent more than 5 μm from source (error rate), see also Figure S10 for error rate across different simulation parameters.

(J) Same data type as (I) for cells navigating in an exponential gradient (fit to interstitial gradient of [I]).

with uniform receptors reached the source within 1 h, compared with 73% of cells (436/600) using the feedback scheme, boosting success rate by more than 30-fold. In fact, Figure 6D shows that > 97% of cells with uniform receptors fail to reach the source even after 6 h, as expected due to being trapped. Improvement in success rate persists across a wide range of scheme parameters (orders-of-magnitude) and directional decoding schemes (Figure S10). We emphasize that the poor performance of cells with uniform receptors is only partially due to inaccuracy associated with decoding local gradients. Indeed, cells that only follow local gradients have trouble finding the global peak (ligand source) in simulated interstitial gradients, as shown by the fact that cells simulated to move precisely along local gradient directions (direction of maximal increase in ligand concentration across the cell's surface) become trapped at local ligand peaks on their way to the source (Figure S10C). As expected, Figure 6E shows that the difference in performance between uniform and scheme-driven receptors is relatively less pronounced in the simple gradient (black curve Figure 6B line plot)—a 2-fold difference in success rate. We discuss the analogy between our feedback scheme and the infotaxis algorithm (Vergassola et al., 2007) in the discussion section.

Our feedback scheme can also help cells remain within a highly precise region along a chemical gradient. During certain developmental programs, cells must restrict their movements within a region along a gradient in order to form stable anatomical structures. GCs demonstrate an extraordinary ability in accomplishing this task. Axon projections of retinal ganglion cells can remain within a band of tissue (lamina) of only 3–7 μm wide, at a specific point along a chemical gradient (Figure 6F) (Xiao and Baier, 2007; Xiao et al., 2011). Figure 6G illustrates how we assess our scheme's ability to achieve this level of precision. We initiate a cell at a gradient source and track the proportion of time the cell was more than 5 μm away from the source. As the cell moves along the gradient, uneven ligand distribution in the environment can lead the cell to move erroneously away from the source. Figure 6H shows that cells with uniform receptors (blue) can indeed make excursions away from the source. However, cells with the feedback scheme (orange) reliably stay close to the source for an extended period of time. We quantify this difference by pooling from 600 trajectories of cells starting at different positions along the source, decoding source direction and navigating for 2 h. Figure 6I shows the number of time steps the cells collectively spent at specific distances from the source. For the circuit parameter values chosen, cells with uniform receptors are found more than 5 μm away from the source 15% of the time (22,204/144,000 steps). On the other hand, cells with the feedback scheme do so only 2% of the time (3,287/144,000 steps), a 7-fold reduction in error rate. Difference in error rate persists for a wide range of scheme parameters and directional decoding schemes (Figures S10D and S10F). Similar improvement in performance is found for cells navigating in fitted exponential gradients (black curve Figure 6G line plot). Figure 6J shows the error rate is reduced by 10-fold from cells with uniform to scheme-driven receptors (10% versus 1%). This result is intuitive as the gradients used for this task has extremely short decay length (5 μm) to mimic *in vivo* gradients that GCs encounter. As a result, the fitted exponential becomes similar to the simulated interstitial gradient. Taken together, our feedback scheme is functionally effective in simulated patchy gradients found in tissue, enabling cells to solve common navigation tasks with substantially improved accuracy and precision.

Optimal efficacy accurately predicts experimental observations of membrane receptor distribution

In addition to generating optimal sensing strategies for simulated environments, our framework can be used to predict receptor distribution of natural cell surface receptors (Figure 7A), using both the environmental structure in which the receptors function and their biological properties. In addition to environmental structure, receptor properties such as cell surface expression level (N) and binding affinity (K_d) also play a role in determining the optimal strategy by affecting the measurement kernel (Equation 3). For a simulated tissue environment, Figure 7B shows that despite offering substantial information gain ($\eta \sim 1$) for a wide range of N and K_d values, optimizing receptor placement offers nearly zero gain in information ($\eta \ll 10^{-2}$) when N/K_d is large. High N and low K_d improve information acquisition by allowing the receptor activities to be more sensitive to changes in input level, and since the total amount of information available to the cell is fixed, the amount of additional gain that can be made by optimizing receptor placement is reduced.

Figure 7B suggests that for real cell surface receptors, we may be able to predict their membrane distribution by specifying both their environment and biological parameters (N, K_d). Specifically for receptors functioning in tissue, we predict those with parameters that fall within the high η regime (Figure 7B) are more likely to adapt the optimal localized distribution. Although data are limited, empirical observations of real receptors agree with this prediction. Comparing data across cell surface receptors from multiple cell types found in human tissue, Figure 7B shows that receptors (red dots) with parameters corresponding to large η have been observed to localize in non-uniform environments (Figures 7Ai–7Aiii). Importantly, the localized receptors concentrate at the region of the membrane with the highest ligand concentration, consistent with the theoretically optimal strategy. Such localization is clearly illustrated in Figures 7Aii and 7Aiii. Figure 7Aii shows, within 5 min, uniform CCR5 redistributes toward the source of CCL5 placed at the bottom edge. Figure 7Aiii shows GABA receptors localize over time to the membrane region experiencing the highest GABA concentration (arrow indicates source direction). Receptors (white dots) with parameters (K_d, N) corresponding to small η, however, are always uniformly distributed (Figure 7Aiv), even when the environment is non-uniform. Furthermore, although Figure 7B is based on a fixed α (constitutive receptor activity), the striking relationship between receptor organization and optimal efficacy η holds for values of α spanning at least two orders-of-magnitude (Figure S11B). More detailed comparisons between the experimental receptor distributions and the theoretical optimum is unfortunately not possible because quantitative descriptions of the ligand profiles experienced by the observed cells are not available. This agreement between theory and observations is not meant to imply that evolution optimizes receptor placement. Indeed, there are key caveats such as variations in receptor expression over time and differences between the environments of different receptors. Our theory does, however, provide a framework for studying natural variations in the spatial organization of receptors, such as differences observed between chemotactic receptors in the same T cell (Nieto et al., 1997).

DISCUSSION

A rich collection of works, spanning diverse areas including developmental biology, systems biology, and neuroscience,

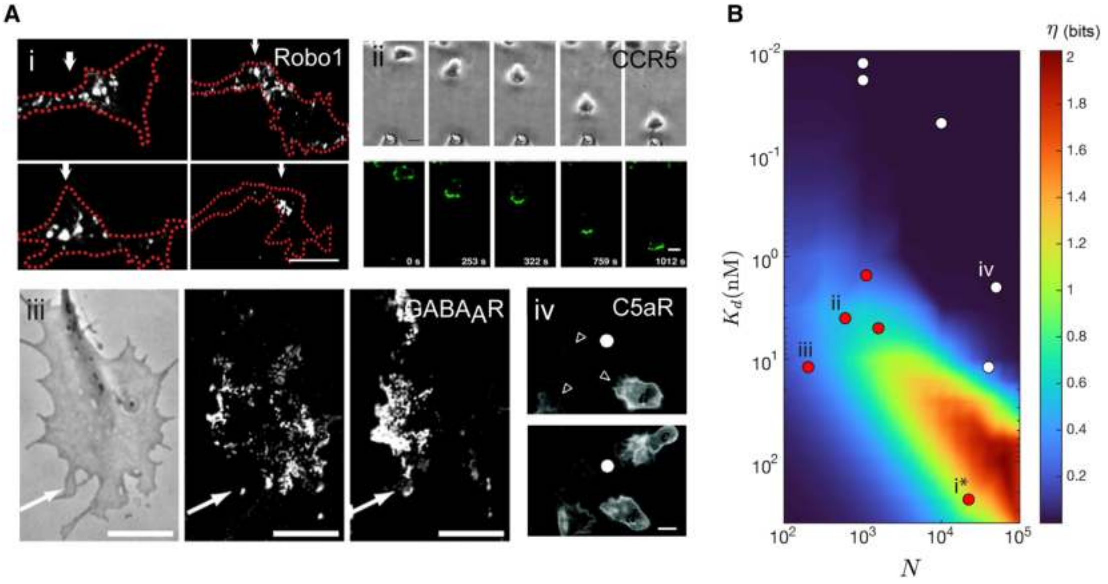

Figure 7. Optimal efficacy η predicts observed distributions of cell surface receptors using their surface expression level and binding affinity

(A) Observed membrane distributions of receptors in heterogeneous environments, (Ai) white arrowheads indicate Slit receptor Robo1 of commissural growth cones navigating in an interstitial Slit gradient (Pignata et al., 2019). (Aii) Human T lymphocytes migrating toward a CCL5-loaded pipette (bottom edge of each panel), top row of panels show brightfield images of a cell taken at different time, bottom row show the corresponding fluorescence images of GFP-tagged CCR5 on the cell surface (time stamp at lower right corner of panel) (Gómez-Moutón et al., 2004), (Aiii) effect of a GABA gradient on the distribution of GABAARs in a growth cone (GC). The arrow indicates direction of the source. (Left) Transmission image of GC. (Center, right) Images show individual quantum dots-tagged GABAARs detected by their fluorescence, recorded during the first 10 min of stimulation (center) and during the next 10 min (right) (Bouzigues et al., 2007), Copyright (2007) National Academy of Sciences, USA. (Aiv) C5aR-GFP remains uniformly distributed in response to a point source of a C5aR agonist, delivered by micropipette (white dot), open arrowheads point to leading edges of cells (Servant et al., 1999). Scale bars: 5 μm in (Ai) and (Aiii) and 10 μm in (Aii) and (Aiv).

(B) Optimal efficacy η for different values of K_d and N; values computed using the tissue environment, where the ratio between average ligand concentration and K_d is fixed, $\alpha = 0.1$; red dots correspond to receptors that polarize in heterogeneous environments (CCR2, CXCR4, CCR5, GABAAR, and Robo1), white dots represent receptors that are constantly uniform (IL-2R, TNFR1, TGFβR2, CR3, and C5aR), roman numerals correspond to receptors in (A), see Table S4 for all receptor data.

put forth the idea of optimizing mutual information to predict the design of information processing systems in biology (Cheong et al., 2011; Dubuis et al., 2013; Monti et al., 2018; Petkova et al., 2019; Sokolowski and Tkačik, 2015; Tkačik et al., 2008, 2009; Tkačik and Gregor, 2021). For example, information maximization principles have been applied to derive fundamental limits on the fidelity of information transfer in biochemical networks (Cheong et al., 2011; Mehta et al., 2009). Inspired by these works, we formulated an information-theoretic framework that enables us to compute effective cell sensing strategies across different environments. We applied the framework to different signaling microenvironments, including tissues and soils, to discover a receptor localization strategy that substantially improves both cell sensing and navigation. More broadly, our work has a series of conceptual and practical implications. Our theory suggests a functional role for spatial organization in cellular information processing, conceptually showing how spatially organized intracellular components can be used by cells to more accurately infer the state of its external environment, here, through sensing and chemoreceptors. Furthermore, our theory conceptually shows how spatial organization of a cell's sensing apparatus can actually reflect spatial structure of its environment. Similar results are found in neuroscience, but it is interesting to see how such an efficient coding perspective can help understand spatial organization within a cell. Lastly, our theory has practical consequences for cell engineering. Currently, most synthetic circuits function without spatial modulation and are studied in well mixed compartments. Our work shows how spatial control over synthetic sense and response architectures can provide new strategies for engineering circuits that function in natural environments.

Adapting framework to optimize other cell properties with respect to environmental statistic

One can easily adapt our framework to understand how variables other than receptor placement affects spatial sensing. Although this work is about optimizing receptor placement, the key quantity being tuned is the spatial distribution of receptor activity; hence, our result is relevant to any variable that (1) affects receptor activity and (2) redistributes across space. To illustrate, consider a generalized model of receptor activation:

$$\mathbb{E}[A_i|c_i] = f(\boldsymbol{\theta}_i)\left(\frac{c_i}{c_i+K_d}+\alpha\frac{K_d}{c_i+K_d}\right), \qquad \text{(Equation 13)}$$

where f is an unspecified function of an arbitrary set of variables $\boldsymbol{\theta}_i$, and $f(\boldsymbol{\theta}_i)$ represents the "effective" number of receptors at position i. In this work, we considered the case where $\theta_i = r_i$ and $f(r_i) = r_i$, but other factors such as phosphorylation level and membrane curvature also affect local receptor activity A_i

(Rangamani et al., 2013). In this way, one can optimize spatial sensing by tuning variables other than receptor placement, by specifying alternative forms of *f*. For example, it is known that given uniformly distributed receptors, those found in membrane regions of higher curvature can exhibit higher activity (Rangamani et al., 2013). Suppose we want to know the optimal way to adjust cell shape to maximize information acquisition, by assuming a linear relationship between local curvature β_i and "effective" receptor number, i.e., $f(r_i, \beta_i) = \beta_i r_i$. Given uniform receptors and a constraint on total contour length (or area) of the membrane, we quickly arrive at the optimal solution since this problem is now identical to our original formulation. The optimal strategy is to increase membrane curvature at regions of high ligand concentration, by making narrow protrusions (STAR Methods).

Connection between information acquisition and navigation

We showed that a receptor placement strategy aimed at maximizing information rate can boost cell navigation performance. Since information content increases toward the ligand source, receptors are more likely to move toward the side of the membrane closer to the source rather than away, enforcing movement up gradients. Furthermore, the trade-off between information acquisition and receptor redistribution in Equation 11 can be viewed as combining exploitative and exploratory tendencies, where larger redistribution "cost" favors exploitation. This strategy is similar in principle to the infotaxis algorithm (Vergassola et al., 2007), where one can view receptors as "navigating agents," whose movements guide the cell toward the target. Although the idea is quite intuitive, the exact relationship between navigation and information acquisition requires further investigation. On the one hand, the feedback scheme is most effective in the case of limited sampling of inputs (Figures S10B and S10E), which suggests maximizing information content indeed helps with navigation. On the other hand, moving receptors to maximize information rate is much more effective as a navigation strategy compared with only maximizing absolute information (Figure S8).

Optimizing spatial organization at different stages of information processing

Optimizing information transmission by organizing effectors in space can happen at all stages of signal processing within the cell but is likely most effective at the receptor level. The most obvious reason is due to the data processing inequality, which states that post-processing cannot increase information. Therefore, only optimization at the level of receptor activation can increase the total amount of information that is available to the cell. The second reason is due to the "hourglass" topology of cell signaling networks, which represent the fact that a large number of signaling inputs converge onto a small number of effectors internal to the cell (Csete and Doyle, 2004). For example, G-protein-coupled receptors, one of the largest group of cell surface receptors, drive downstream signaling through the same G proteins. This feature makes optimizing spatial organization at later stages of information processing very difficult, since information can be easily lost by diffusion of effector molecules activated by different inputs, which ends up "mixing" different spatial signals.

STAR★METHODS

Detailed methods are provided in the online version of this paper and include the following:

- KEY RESOURCES TABLE
- RESOURCE AVAILABILITY
  - ○ Lead contact
  - ○ Materials availability
  - ○ Data and code availability
- METHOD DETAILS
  - ○ Formulation of optimization problem
  - ○ Theoretical properties of Poisson channels
  - ○ Factors affecting optimal receptor placement
  - ○ Chemical microenvironment models
  - ○ Dynamic protocol for receptor rearrangement
  - ○ Numerical simulation of receptor feedback scheme
  - ○ Simulation of cell navigation
  - ○ Extensions of framework to other strategies

SUPPLEMENTAL INFORMATION

Supplemental information can be found online at https://doi.org/10.1016/j.cels.2022.05.004.

ACKNOWLEDGMENTS

We thank Michael Elowitz, Erik Winfree, and David Sivak for scientific discussions; Dominik Schildknecht, Han Kim, Guruprasad Raghavan, Pranav Bhamidipati, Abdullah Farooq for feedback on the manuscript; Inna-Marie Strazhnik for illustrations; and Angela Anderson for editorial advice. We also would like to thank Eugenio Marco and Katarzyna Rejniak for technical advice with receptor feedback and tissue simulations, respectively. The authors would like to acknowledge the Heritage Medical Research Institute and Packard Foundation for funding and intellectual support.

AUTHOR CONTRIBUTIONS

Conceptualization, Z.J.W. and M.T.; methodology, Z.J.W. and M.T.; manuscript writing, Z.J.W. and M.T.; supervision, M.T.; funding acquisition, M.T.

DECLARATION OF INTERESTS

M.T. is a member of the advisory board of *Cell Systems*.

Received: November 5, 2021
Revised: February 8, 2022
Accepted: May 12, 2022
Published: June 8, 2022

SUPPORTING CITATIONS

The following references appear in the supplemental information: Berger et al., (1984); Cai and Wright, (1995); Caruncho et al., (1995); Evans and Bashaw, (2010); Fitzgerald et al., (2001); Gehr et al., (1992); Grell et al., (1998); Höfer et al., (2012); Huey and Hugli, (1985); Jones et al., (1998); Komatsu et al., (2017); Lee et al., (1999); Marchetti et al., (2013); Martínez-Muñoz et al., (2018); Miller et al., (2018); Pelletier et al., (2000); Pytowski et al., (1990); Qing et al., (2020); Ren et al., (2014); RStudio Team, (2015); Shields et al., (2007); Swartz and Fleury, (2007); Thoma et al., (1990); Tripathi et al., 91993); Tucker et al., (1984); Wang and Irvine, (2013); Yoshimura, (2018).

REFERENCES

Baddeley, A., Rubak, E., and Turner, R. (2015). Spatial Point Patterns: Methodology and Applications with R (Chapman & Hall/CRC Press). http://

www.crcpress.com/Spatial-Point-Patterns-Methodology-and-Applications-with-R/Baddeley-Rubak-Turner/9781482210200/.

Belema-Bedada, F., Uchida, S., Martire, A., Kostin, S., and Braun, T. (2008). Efficient homing of multipotent adult mesenchymal stem cells depends on frount-mediated clustering of ccr2. Cell Stem Cell *2*, 566–575.

Berg, H.C., and Purcell, E.M. (1977). Physics of chemoreception. Biophys. J. *20*, 193–219.

Berger, M., O'Shea, J., Cross, A.S., Folks, T.M., Chused, T.M., Brown, E.J., and Frank, M.M. (1984). Human neutrophils increase expression of c3bi as well as c3b receptors upon activation. J. Clin. Invest. *74*, 1566–1571.

Bouzigues, C., Morel, M., Triller, A., and Dahan, M. (2007). Asymmetric redistribution of gaba receptors during gaba gradient sensing by nerve growth cones analyzed by single quantum dot imaging. Proc. Natl. Acad. Sci. USA *104*, 11251–11256.

Buchwald, P. (2019). A receptor model with binding affinity, activation efficacy, and signal amplification parameters for complex fractional response versus occupancy data. Front. Pharmacol. *10*, 605.

Burton, E.O., Read, H.W., Pellitteri, M.C., and Hickey, W.J. (2005). Identification of acyl-homoserine lactone signal molecules produced by Nitrosomonas europaea strain schmidt. Appl. Environ. Microbiol. *71*, 4906–4909.

Cai, T.-Q., and Wright, S.D. (1995). Energetics of leukocyte integrin activation. J. Biol. Chem. *270*, 14358–14365.

Candès, E.J., and Wakin, M.B. (2008). An introduction to compressive sampling. IEEE Signal Process. Mag. *25*, 21–30.

Caruncho, H.J., Puia, G., Mohler, H., and Costa, E. (1995). The density and distribution of six GABAA receptor subunits in primary cultures of rat cerebellar granule cells. Neuroscience *67*, 583–593.

Caselton, W.F., and Zidek, J.V. (1984). Optimal monitoring network designs. Stat. Probab. Lett. *2*, 223–227.

Chau, A.H., Walter, J.M., Gerardin, J., Tang, C., and Lim, W.A. (2012). Designing synthetic regulatory networks capable of self-organizing cell polarization. Cell *151*, 320–332.

Cheong, R., Rhee, A., Wang, C.J., Nemenman, I., and Levchenko, A. (2011). Information transduction capacity of noisy biochemical signaling networks. Science *334*, 354–358.

Chou, C.-S., Bardwell, L., Nie, Q., and Yi, T.-M. (2011). Noise filtering tradeoffs in spatial gradient sensing and cell polarization response. BMC Syst. Biol. *5*, 196.

Clark, K.E., Lopez, H., Abdi, B.A., Guerra, S.G., Shiwen, X., Khan, K., Etomi, O., Martin, G.R., Abraham, D.J., Denton, C.P., et al. (2015). Multiplex cytokine analysis of dermal interstitial blister fluid defines local disease mechanisms in systemic sclerosis. Arthritis Res. Ther. *17*, 73.

Csete, M., and Doyle, J. (2004). Bow ties, metabolism and disease. Trends Biotechnol. *22*, 446–450.

de Anna, P., Pahlavan, A.A., Yawata, Y., Stocker, R., and Juanes, R. (2021). Chemotaxis under flow disorder shapes microbial dispersion in porous media. Nat. Phys. *17*, 68–73.

Diz-Muñoz, A., Thurley, K., Chintamen, S., Altschuler, S.J., Wu, L.F., Fletcher, D.A., and Weiner, O.D. (2016). Membrane tension acts through pld2 and mtorc2 to limit actin network assembly during neutrophil migration. PLoS Biol. *14*, e1002474.

Dlamini, M., Kennedy, T.E., and Juncker, D. (2020). Combinatorial nanodot stripe assay to systematically study cell haptotaxis. Microsyst. Nanoeng. *6*, 114.

Dubuis, J.O., Tkačik, G., Wieschaus, E.F., Gregor, T., and Bialek, W. (2013). Positional information, in bits. Proc. Natl. Acad. Sci. USA *110*, 16301–16308.

Dytso, A., Faus, M., and Poor, H.V. (2020). The vector poisson channel: on the linearity of the conditional mean estimator. IEEE Trans. Signal Process. *68*, 5894–5903.

Endres, R.G., and Wingreen, N.S. (2008). Accuracy of direct gradient sensing by single cells. Proc. Natl. Acad. Sci. USA *105*, 15749–15754.

Evans, T.A., and Bashaw, G.J. (2010). Functional diversity of robo receptor immunoglobulin domains promotes distinct axon guidance decisions. Curr. Biol. *20*, 567–572.

Fitzgerald, K.A., O'Neill, L.A., Gearing, A.J., and Callard, R.E. (2001). The Cytokine Factsbook and Webfacts (Elsevier).

Fowell, D.J., and Kim, M. (2021). The spatio-temporal control of effector T cell migration. Nat. Rev. Immunol. *21*, 582–596.

Friedl, P., Maaser, K., Klein, C.E., Niggemann, B., Krohne, G., and Zänker, K.S. (1997). Migration of highly aggressive mv3 melanoma cells in 3-dimensional collagen lattices results in local matrix reorganization and shedding of $\alpha 2$ and $\beta 1$ integrins and CD44. Cancer Res. *57*, 2061–2070.

Gantner, S., Schmid, M., Dürr, C., Schuhegger, R., Steidle, A., Hutzler, P., Langebartels, C., Eberl, L., Hartmann, A., and Dazzo, F.B. (2006). In situ quantitation of the spatial scale of calling distances and population density-independent n-acylhomoserine lactone-mediated communication by rhizobacteria colonized on plant roots. FEMS Microbiol. Ecol. *56*, 188–194.

Gehr, G., Gentz, R., Brockhaus, M., Loetscher, H., and Lesslauer, W. (1992). Both tumor necrosis factor receptor types mediate proliferative signals in human mononuclear cell activation. J. Immunol. *149*, 911–917.

Gómez-Moutón, C., Lacalle, R.A., Mira, E., Jiménez-Baranda, S., Barber, D.F., Carrera, A.C., Martínez-A, C., and Mañes, S. (2004). Dynamic redistribution of raft domains as an organizing platform for signaling during cell chemotaxis. J. Cell Biol. *164*, 759–768.

Grell, M., Wajant, H., Zimmermann, G., and Scheurich, P. (1998). The type 1 receptor (CD120a) is the high-affinity receptor for soluble tumor necrosis factor. Proc. Natl. Acad. Sci. USA *95*, 570–575.

Guo, D., Shamai, S., and Verdú, S. (2008). Mutual information and conditional mean estimation in poisson channels. IEEE Trans. Inf. Theor. *54*, 1837–1849.

Harjanto, D., and Zaman, M.H. (2013). Modeling extracellular matrix reorganization in 3-d environments. PLoS One *8*, e52509.

Hegemann, B., Unger, M., Lee, S.S., Stoffel-Studer, I., van den Heuvel, J., Pelet, S., Koeppl, H., and Peter, M. (2015). A cellular system for spatial signal decoding in chemical gradients. Dev. Cell *35*, 458–470.

Hodge, A. (2006). Plastic plants and patchy soils. J. Exp. Bot. *57*, 401–411.

Höfer, T., Krichevsky, O., and Altan-Bonnet, G. (2012). Competition for IL-2 between regulatory and effector T cells to chisel immune responses. Front. Immunol. *3*, 268.

Hu, B., Chen, W., Rappel, W.-J., and Levine, H. (2010). Physical limits on cellular sensing of spatial gradients. Phys. Rev. Lett. *105*, 048104.

Huey, R., and Hugli, T.E. (1985). Characterization of a C5a receptor on human polymorphonuclear leukocytes (pmn). J. Immunol. *135*, 2063–2068.

Huston, S.J., Stopfer, M., Cassenaer, S., Aldworth, Z.N., and Laurent, G. (2015). Neural encoding of odors during active sampling and in turbulent plumes. Neuron *88*, 403–418.

Iida, F., and Nurzaman, S.G. (2016). Adaptation of sensor morphology: an integrative view of perception from biologically inspired robotics perspective. Interface Focus *6*, 20160016.

Jones, M.V., Sahara, Y., Dzubay, J.A., and Westbrook, G.L. (1998). Defining affinity with the GABAA receptor. J. Neurosci. *18*, 8590–8604.

Kennedy, T.E., Wang, H., Marshall, W., and Tessier-Lavigne, M. (2006). Axon guidance by diffusible chemoattractants: a gradient of netrin protein in the developing spinal cord. J. Neurosci. *26*, 8866–8874.

Kicheva, A., Pantazis, P., Bollenbach, T., Kalaidzidis, Y., Bittig, T., Jülicher, F., and González-Gaitán, M. (2007). Kinetics of morphogen gradient formation. Science *315*, 521–525.

Kinoshita-Kawada, M., Hasegawa, H., Hongu, T., Yanagi, S., Kanaho, Y., Masai, I., Mishima, T., Chen, X., Tsuboi, Y., Rao, Y., et al. (2019). A crucial role for arf6 in the response of commissural axons to slit. Development *146*, dev172106.

Koenig, J.A., and Edwardson, J.M. (1994). Kinetic analysis of the trafficking of muscarinic acetylcholine receptors between the plasma membrane and intracellular compartments. J. Biol. Chem. *269*, 17174–17182.

Koenig, J.A., and Edwardson, J.M. (1996). Intracellular trafficking of the muscarinic acetylcholine receptor: importance of subtype and cell type. Mol. Pharmacol. *49*, 351–359.

Komatsu, N., Mitsui, K., Kusano Arai, O., Iwanari, H., Hoshi, K., Takato, T., Abe, T., and Hamakubo, T. (2017). Enhancement of anti-robo1 immunotoxin cytotoxicity to head and neck squamous cell carcinoma via photochemical internalization. Arch. Cancer Res. *05*.

Krause, A., Singh, A., and Guestrin, C. (2008). Near-optimal sensor placements in gaussian processes: theory, efficient algorithms and empirical studies. J. Mach. Learn. Res. *9*.

Lauffenburger, D.A., and Linderman, J.J. (1993). Receptors: Models for Binding, Trafficking, and Signaling (Oxford University Press).

Lee, B., Sharron, M., Montaner, L.J., Weissman, D., and Doms, R.W. (1999). Quantification of CD4, ccr5, and cxcr4 levels on lymphocyte subsets, dendritic cells, and differentially conditioned monocyte-derived macrophages. Proc. Natl. Acad. Sci. USA *96*, 5215–5220.

Lee, B., Zhou, X., Riching, K., Eliceiri, K.W., Keely, P.J., Guelcher, S.A., Weaver, A.M., and Jiang, Y. (2014). A three-dimensional computational model of collagen network mechanics. PloS One *9*, e111896.

Lim, K., Hyun, Y.-M., Lambert-Emo, K., Capece, T., Bae, S., Miller, R., Topham, D.J., and Kim, M. (2015). Neutrophil trails guide influenza-specific CD8+ T cells in the airways. Science *349*, aaa4352.

Macara, I.G., and Mili, S. (2008). Polarity and differential inheritance—universal attributes of life? Cell *135*, 801–812.

Majzner, R.G., Rietberg, S.P., Sotillo, E., Dong, R., Vachharajani, V.T., Labanieh, L., Myklebust, J.H., Kadapakkam, M., Weber, E.W., Tousley, A.M., et al. (2020). Tuning the antigen density requirement for car T-cell activity. Cancer Discov. *10*, 702–723.

Marchetti, L., Callegari, A., Luin, S., Signore, G., Viegi, A., Beltram, F., and Cattaneo, A. (2013). Ligand signature in the membrane dynamics of single trka receptor molecules. J. Cell Sci. *126*, 4445–4456.

Marco, E., Wedlich-Soldner, R., Li, R., Altschuler, S.J., and Wu, L.F. (2007). Endocytosis optimizes the dynamic localization of membrane proteins that regulate cortical polarity. Cell *129*, 411–422.

Martinez, M., and Moon, E.K. (2019). CAR T cells for solid tumors: new strategies for finding, infiltrating, and surviving in the tumor microenvironment. Front. Immunol. *10*, 128.

Martínez-Muñoz, L., Rodríguez-Frade, J.M., Barroso, R., Sorzano, C.Ó.S., Torreño-Pina, J.A., Santiago, C.A., Manzo, C., Lucas, P., García-Cuesta, E.M., Gutierrez, E., et al. (2018). Separating actin-dependent chemokine receptor nanoclustering from dimerization indicates a role for clustering in cxcr4 signaling and function. Mol. Cell *70*, 106–119.e10.

MATLAB Optimization Toolbox (2021a). The MathWorks, Natick, MA, USA.

Mehta, P., Goyal, S., Long, T., Bassler, B.L., and Wingreen, N.S. (2009). Information processing and signal integration in bacterial quorum sensing. Mol. Syst. Biol. *5*, 325.

Melke, P., Sahlin, P., Levchenko, A., and Jönsson, H. (2010). A cell-based model for quorum sensing in heterogeneous bacterial colonies. PLoS Comp. Biol. *6*, e1000819.

Milde, F., Bergdorf, M., and Koumoutsakos, P. (2008). A hybrid model for three-dimensional simulations of sprouting angiogenesis. Biophys. J. *95*, 3146–3160.

Miller, H., Cosgrove, J., Wollman, A.J.M., Taylor, E., Zhou, Z., O'Toole, P.J., Coles, M.C., and Leake, M.C. (2018). High-speed single-molecule tracking of CXCL13 in the b-follicle. Front. Immunol. *9*, 1073.

Monti, M., Lubensky, D.K., and Ten Wolde, P.R. (2018). Optimal entrainment of circadian clocks in the presence of noise. Phys. Rev. E *97*, 032405.

Mossman, K.D., Campi, G., Groves, J.T., and Dustin, M.L. (2005). Altered tcr signaling from geometrically repatterned immunological synapses. Science *310*, 1191–1193.

Mugler, A., Levchenko, A., and Nemenman, I. (2016). Limits to the precision of gradient sensing with spatial communication and temporal integration. Proc. Natl. Acad. Sci. USA *113*, E689–E695.

Nieto, M., Frade, J.M., Sancho, D., Mellado, M., Martinez-A, C., and Sánchez-Madrid, F. (1997). Polarization of chemokine receptors to the leading edge during lymphocyte chemotaxis. J. Exp. Med. *186*, 153–158.

Nunan, N., Ritz, K., Crabb, D., Harris, K., Wu, K., Crawford, J.W., and Young, I.M. (2001). Quantification of the in situ distribution of soil bacteria by large-scale imaging of thin sections of undisturbed soil. FEMS Microbiol. Ecol. *37*, 67–77.

Pelletier, A.J., van der Laan, L.J., Hildbrand, P., Siani, M.A., Thompson, D.A., Dawson, P.E., Torbett, B.E., and Salomon, D.R. (2000). Presentation of chemokine sdf-1α by fibronectin mediates directed migration of T cells, Blood. J. Am. Soc. Hematol. *96*, 2682–2690.

Petkova, M.D., Tkačik, G., Bialek, W., Wieschaus, E.F., and Gregor, T. (2019). Optimal decoding of cellular identities in a genetic network. Cell *176*, 844–855.e15.

Pignata, A., Ducuing, H., Boubakar, L., Gardette, T., Kindbeiter, K., Bozon, M., Tauszig-Delamasure, S., Falk, J., Thoumine, O., and Castellani, V. (2019). A spatiotemporal sequence of sensitization to slits and semaphorins orchestrates commissural axon navigation. Cell Rep. *29*, 347–362.e5.

Pippig, S., Andexinger, S., and Lohse, M.J. (1995). Sequestration and recycling of beta 2-adrenergic receptors permit receptor resensitization. Mol. Pharmacol. *47*, 666–676.

Pytowski, B., Maxfield, F.R., and Michl, J. (1990). Fc and c3bi receptors and the differentiation antigen bh2-ag are randomly distributed in the plasma membrane of locomoting neutrophils. J. Cell Biol. *110*, 661–668.

Qing, R., Tao, F., Chatterjee, P., Yang, G., Han, Q., Chung, H., Ni, J., Suter, B.P., Kubicek, J., Maertens, B., et al. (2020). Non-full-length water-soluble cxcr4qty and ccr5qty chemokine receptors: implication for overlooked truncated but functional membrane receptors. Iscience *23*, 101670.

Rabin, J., Delon, J., and Gousseau, Y. (2011). Transportation distances on the circle. J. Math. Imaging Vision *41*, 147–167.

Rangamani, P., Lipshtat, A., Azeloglu, E.U., Calizo, R.C., Hu, M., Ghassemi, S., Hone, J., Scarlata, S., Neves, S.R., and Iyengar, R. (2013). Decoding information in cell shape. Cell *154*, 1356–1369.

Raynaud, X., and Nunan, N. (2014). Spatial ecology of bacteria at the microscale in soil. PloS One *9*, e87217.

Rejniak, K.A., Estrella, V., Chen, T., Cohen, A.S., Lloyd, M.C., and Morse, D.L. (2013). The role of tumor tissue architecture in treatment penetration and efficacy: an integrative study. Front. Oncol. *3*, 111.

Ren, A., Moon, C., Zhang, W., Sinha, C., Yarlagadda, S., Arora, K., Wang, X., Yue, J., Parthasarathi, K., Heil-Chapdelaine, R., et al. (2014). Asymmetrical macromolecular complex formation of lysophosphatidic acid receptor 2 (lpa2) mediates gradient sensing in fibroblasts. J. Biol. Chem. *289*, 35757–35769.

RStudio Team (2015). RStudio: Integrated Development Environment for R (R.Studio Inc.). http://www.rstudio.com/.

Russo, E., Teijeira, A., Vaahtomeri, K., Willrodt, A.H., Bloch, J.S., Nitschké, M., Santambrogio, L., Kerjaschki, D., Sixt, M., and Halin, C. (2016). Intralymphatic CCL21 promotes tissue egress of dendritic cells through afferent lymphatic vessels. Cell Rep. *14*, 1723–1734.

Sarris, M., Masson, J.-B., Maurin, D., Van der Aa, L.M., Boudinot, P., Lortat-Jacob, H., and Herbomel, P. (2012). Inflammatory chemokines direct and restrict leukocyte migration within live tissues as glycan-bound gradients. Curr. Biol. *22*, 2375–2382.

Schlather, M., Malinowski, A., Oesting, M., Boecker, D., Strokorb, K., Engelke, S., Martini, J., Ballani, F., Moreva, O., Auel, J., et al. (2020). RandomFields: simulation and analysis of random fields. R package version 3.3.8. https://cran.r-project.org/package=RandomFields.

Schlüter, D.K., Ramis-Conde, I., and Chaplain, M.A. (2012). Computational modeling of single-cell migration: the leading role of extracellular matrix fibers. Biophys. J. *103*, 1141–1151.

Seifert, R., and Wenzel-Seifert, K. (2002). Constitutive activity of G-protein-coupled receptors: cause of disease and common property of wild-type receptors. Naunyn-Schmiedebergs Arch. Pharmacol. *366*, 381–416.

Servant, G., Weiner, O.D., Neptune, E.R., Sedat, J.W., and Bourne, H.R. (1999). Dynamics of a chemoattractant receptor in living neutrophils during chemotaxis. Mol. Biol. Cell *10*, 1163–1178.

Sheng, H., Song, Y., Bian, Y., Wu, W., Xiang, L., Liu, G., Jiang, X., and Wang, F. (2017). Determination of n-acyl homoserine lactones in soil using accelerated solvent extraction combined with solid-phase extraction and gas chromatography-mass spectrometry. Anal. Methods *9*, 688–696.

Shields, J.D., Fleury, M.E., Yong, C., Tomei, A.A., Randolph, G.J., and Swartz, M.A. (2007). Autologous chemotaxis as a mechanism of tumor cell homing to lymphatics via interstitial flow and autocrine ccr7 signaling. Cancer Cell *11*, 526–538.

Shimonaka, M., Katagiri, K., Nakayama, T., Fujita, N., Tsuruo, T., Yoshie, O., and Kinashi, T. (2003). Rap1 translates chemokine signals to integrin activation, cell polarization, and motility across vascular endothelium under flow. J. Cell Biol. *161*, 417–427.

Slack, R.J., and Hall, D.A. (2012). Development of operational models of receptor activation including constitutive receptor activity and their use to determine the efficacy of the chemokine CCL17 at the cc chemokine receptor ccr4. Br. J. Pharmacol. *166*, 1774–1792.

Sokolowski, T.R., and Tkačik, G. (2015). Optimizing information flow in small genetic networks. Phys. Rev. E *91*, 062710.

Suchkov, D.V., DeFlorio, R., Draper, E., Ismael, A., Sukumar, M., Arkowitz, R., and Stone, D.E. (2010). Polarization of the yeast pheromone receptor requires its internalization but not actin-dependent secretion. Mol. Biol. Cell *21*, 1737–1752.

Swartz, M.A., and Fleury, M.E. (2007). Interstitial flow and its effects in soft tissues. Annu. Rev. Biomed. Eng. *9*, 229–256.

Thoma, B., Grell, M., Pfizenmaier, K., and Scheurich, P. (1990). Identification of a 60-kd tumor necrosis factor (tnf) receptor as the major signal transducing component in tnf responses. J. Exp. Med. *172*, 1019–1023.

Tkačik, G., Callan, C.G., and Bialek, W. (2008). Information flow and optimization in transcriptional regulation. Proc. Natl. Acad. Sci. USA *105*, 12265–12270.

Tkačik, G., and Gregor, T. (2021). The many bits of positional information. Development *148*, dev176065.

Tkačik, G., Walczak, A.M., and Bialek, W. (2009). Optimizing information flow in small genetic networks. Phys. Rev. E Stat. Nonlin. Soft Matter Phys. *80*, 031920.

Tripathi, R.C., Borisuth, N.S., Kolli, S.P., and Tripathi, B.J. (1993). Trabecular cells express receptors that bind TGF-beta 1 and TGF-beta 2: a qualitative and quantitative characterization. Invest. Ophthalmol. Vis. Sci. *34*, 260–263.

Tucker, R.F., Branum, E.L., Shipley, G.D., Ryan, R.J., and Moses, H.L. (1984). Specific binding to cultured cells of 125i-labeled type beta transforming growth factor from human platelets. Proc. Natl. Acad. Sci. USA *81*, 6757–6761.

Ueda, M., Sako, Y., Tanaka, T., Devreotes, P., and Yanagida, T. (2001). Single-molecule analysis of chemotactic signaling in Dictyostelium cells. Science *294*, 864–867.

van Buul, J.D., Voermans, C., van Gelderen, J., Anthony, E.C., van der Schoot, C.E., and Hordijk, P.L. (2003). Leukocyte-endothelium interaction promotes sdf-1-dependent polarization of cxcr4. J. Biol. Chem. *278*, 30302–30310.

Vergassola, M., Villermaux, E., and Shraiman, B.I. (2007). 'infotaxis' as a strategy for searching without gradients. Nature *445*, 406–409.

Vicente-Manzanares, M., and Sánchez-Madrid, F. (2004). Role of the cytoskeleton during leukocyte responses. Nat. Rev. Immunol. *4*, 110–122.

von Philipsborn, A.C., Lang, S., Loeschinger, J., Bernard, A., David, C., Lehnert, D., Bonhoeffer, F., and Bastmeyer, M. (2006). Growth cone navigation in substrate-bound ephrin gradients. Development *133*, 2487–2495.

Wang, L., Carlson, D.E., Rodrigues, M.R.D., Calderbank, R., and Carin, L. (2014). A Bregman matrix and the gradient of mutual information for vector poisson and Gaussian channels. IEEE Trans. Inf. Theor. *60*, 2611–2629.

Wang, X., Lennartz, M.R., Loegering, D.J., and Stenken, J.A. (2008). Multiplexed cytokine detection of interstitial fluid collected from polymeric hollow tube implants—a feasibility study. Cytokine *43*, 15–19.

Wang, X., Tian, W., Banh, B.T., Statler, B.-M., Liang, J., and Stone, D.E. (2019). Mating yeast cells use an intrinsic polarity site to assemble a pheromone-gradient tracking machine. J. Cell Biol. *218*, 3730–3752.

Wang, Y., and Irvine, D.J. (2013). Convolution of chemoattractant secretion rate, source density, and receptor desensitization direct diverse migration patterns in leukocytes. Integr. Biol. (Camb) *5*, 481–494.

Wang, Y.-J., and Leadbetter, J.R. (2005). Rapid acyl-homoserine lactone quorum signal biodegradation in diverse soils. Appl. Environ. Microbiol. *71*, 1291–1299.

Weber, M., Hauschild, R., Schwarz, J., Moussion, C., De Vries, I., Legler, D.F., Luther, S.A., Bollenbach, T., and Sixt, M. (2013). Interstitial dendritic cell guidance by haptotactic chemokine gradients. Science *339*, 328–332.

Xiao, T., and Baier, H. (2007). Lamina-specific axonal projections in the zebrafish tectum require the type iv collagen dragnet. Nat. Neurosci. *10*, 1529–1537.

Xiao, T., Staub, W., Robles, E., Gosse, N.J., Cole, G.J., and Baier, H. (2011). Assembly of lamina-specific neuronal connections by slit bound to type iv collagen. Cell *146*, 164–176.

Yang, B.-G., Tanaka, T., Jang, M.H., Bai, Z., Hayasaka, H., and Miyasaka, M. (2007). Binding of lymphoid chemokines to collagen iv that accumulates in the basal lamina of high endothelial venules: its implications in lymphocyte trafficking. J. Immunol. *179*, 4376–4382.

Yokosuka, T., Sakata-Sogawa, K., Kobayashi, W., Hiroshima, M., Hashimoto-Tane, A., Tokunaga, M., Dustin, M.L., and Saito, T. (2005). Newly generated T cell receptor microclusters initiate and sustain T cell activation by recruitment of zap70 and slp-76. Nat. Immunol. *6*, 1253–1262.

Yoshimura, T. (2018). The chemokine mcp-1 (ccl2) in the host interaction with cancer: a foe or ally? Cell. Mol. Immunol. *15*, 335–345.

Zhu, M., Cornwall-Scoones, J., Wang, P., Handford, C.E., Na, J., Thomson, M., and Zernicka-Goetz, M. (2020). Developmental clock and mechanism of de novo polarization of the mouse embryo. Science *370*, eabd2703.

STAR★METHODS

KEY RESOURCES TABLE

REAGENT or RESOURCE	SOURCE	IDENTIFIER
Deposited data		
All computationally generated data, analysis scripts and plotting scripts	This paper	CaltechDATA: https://doi.org/10.22002/D1.2149
Image of cell surface Robo1 distribution	Pignata et al., 2019	https://doi.org/10.1016/j.celrep.2019.08.098
Image of cell surface CCR5 distribution	Gómez-Moutón et al., 2004	https://doi.org/10.1083/jcb.200309101
Image of cell surface GABAAR distribution	Bouzigues et al. 2007	https://doi.org/10.1073/pnas.0702536104
Image of cell surface C5aR distribution	Servant et al., 1999	https://doi.org/10.1091/mbc.10.4.1163
Software and algorithms		
Matlab R2020b	Mathworks	RRID:SCR_001622
RStudio v1.3	RStudio	RRID:SCR_000432
Analysis and figure scripts	This paper	Zenodo: https://doi.org/10.5281/zenodo.6432083

RESOURCE AVAILABILITY

Lead contact

Further information and requests for resources should be directed to and will be fulfilled by the lead contact, Matt Thomson (mthomson@caltech.edu).

Materials availability

This study did not generate new materials.

Data and code availability

- All data have been deposited on the Caltech Research Data Repository and are publicly available as of the date of publication. DOIs are listed in the key resources table.
- All original code has been deposited at Zenodo (10.5281/zenodo.6432083) and is publicly available as of the date of publication. DOIs are listed in the key resources table.
- Any additional information required to reanalyze the data reported in this paper is available from the lead contact upon request.

METHOD DETAILS

Formulation of optimization problem

In this paper, we developed a theoretical framework to study whether manipulating the placement of cell surface receptors can improve the spatial sensing performance. Optimizing spatial sensing by tuning receptor placement is analogous to optimizing distributed electronic sensor network by adjusting the location of sensors, which has been extensively studied in signal processing (Krause et al., 2008). Before presenting the general optimization problem, we set up the mathematical framework through the lens of information theory. Consider a two-dimensional (2D) cell with a 1D membrane surface. By discretizing the membrane into m equally-sized regions, we modeled the membrane receptor system as m parallel communication channels (Figure 1B). The i-th channel takes as input $C_i \in \mathbb{N}_0$, a random variable denoting ligand count at the i-th region of the membrane surface. Given $r_i \in \mathbb{N}_0$ receptors, this channel produces as output $A_i \in \mathbb{N}_0$, a number of active receptors that is random due to stochastic nature of receptor activation and randomness in C_i. Given m channels representing the entire cell membrane, our model comprised four key mathematical objects: ligand profile $\boldsymbol{C} = (C_1,\dots,C_m)$, receptor placement $\boldsymbol{r} = (r_1,..,r_m)$, active receptor profile $\boldsymbol{A} = (A_1,\dots,A_m)$, and measurement kernel $P(\boldsymbol{A} = \boldsymbol{a}|\boldsymbol{C} = \boldsymbol{c},\boldsymbol{r})$. The input $\boldsymbol{C} \sim p(\boldsymbol{c})$ is now the entire ligand profile across the cell surface. Each realization $\boldsymbol{c}$ of $\boldsymbol{C}$ has probability $p(\boldsymbol{c})$ of being observed. We explain below how $p(\boldsymbol{c})$ can be constructed to represent statistics of ligand profiles cells naturally encounter (see input statistic). The receptor profile $\boldsymbol{r}$ denotes the number of receptor allocated to each membrane region. The output $\boldsymbol{A} \sim p(\boldsymbol{a})$ is the number of active receptors across the membrane, which depends on $\boldsymbol{c}$ and $\boldsymbol{r}$ through $p(\boldsymbol{a}|\boldsymbol{c},\boldsymbol{r})$, the measurement kernel. We explain below how this kernel can be modeled (see measurement kernel).

Consider a placement strategy $\varphi : \boldsymbol{c} \rightarrow \boldsymbol{r}$, that maps a ligand profile to a receptor placement. In our general optimization problem (Figure 1B), we are interested in the choice of φ that maximizes the amount of information the cell can obtain regarding $\boldsymbol{C}$ by observing $\boldsymbol{A}$, for a fixed number of receptors N. Formally, we quantify this information using the mutual information,

$$I(\boldsymbol{C};\boldsymbol{A}) = \sum_{\boldsymbol{c}\in\boldsymbol{C}}\sum_{\boldsymbol{a}\in\boldsymbol{A}} p(\boldsymbol{c},\boldsymbol{a})\log\frac{p(\boldsymbol{c},\boldsymbol{a})}{p(\boldsymbol{c})p(\boldsymbol{a})}. \tag{Equation 14}$$

The mutual information is minimized when $\boldsymbol{C}$ and $\boldsymbol{A}$ are independent, and maximized when one is a deterministic function of the other. Since $p(\boldsymbol{c},\boldsymbol{a}) = p(\boldsymbol{a}|\boldsymbol{c},\boldsymbol{r} = \varphi(\boldsymbol{c}))p(\boldsymbol{c})$, each summand in the mutual information will be affected by the choice of φ. Taken together, we arrive at our general formulation of the optimal strategy φ^*:

$$\varphi^*_{p(\boldsymbol{c})} = \underset{\substack{\forall\boldsymbol{c}\ \varphi(\boldsymbol{c})\geq 0 \\ \sum_i \varphi_i(\boldsymbol{c}) = N}}{\operatorname{argmax}}\ I(\boldsymbol{C};\boldsymbol{A}|\varphi,\ p(\boldsymbol{c})), \tag{Equation 15}$$

where N is the total number of receptors. The subscript $p(\boldsymbol{c})$ is meant to emphasize the dependence of the optimal strategy on the input statistics.

To solve for $\varphi^*_{p(\boldsymbol{c})}$, we needed to specify both a measurement kernel $p(\boldsymbol{a}|\boldsymbol{c},\boldsymbol{r})$ and an input statistic $p(\boldsymbol{c})$. The input statistic $p(\boldsymbol{c})$ for an environment represents the probability that a cell in that environment will encounter the ligand profile $\boldsymbol{c}$.

Measurement kernel

We model $p(\boldsymbol{a}|\boldsymbol{c},\boldsymbol{r})$ assuming that each receptor binds ligands locally and activates independently of other receptors. These assumptions allow us to factorize $p(\boldsymbol{a}|\boldsymbol{c},\boldsymbol{r})$ as follows,

$$P(\boldsymbol{A} = \boldsymbol{a}|\boldsymbol{C} = \boldsymbol{c},\ \boldsymbol{r}) = \prod_{i=1}^{m} P(A_i = a_i|C_i = c_i,\ r_i). \tag{Equation 16}$$

Each local sensing process involves probabilistic ligand-receptor interaction which can be viewed as a Bernoulli process. In this way, the number of active receptors follows a Binomial distribution, which can be approximated with the Poisson distribution when the probability of successful binding event is low. Indeed, experimental measurements have shown that receptor occupancy is well-approximated by the Poisson distribution (Ueda et al., 2001), such that

$$P(A_i = a_i|C_i = c_i,\ r_i) = \frac{{\mu_i}^{a_i}}{a_i!}e^{-\mu_i}, \tag{Equation 17}$$

where $\mu_i = r_i\left(\frac{c_i}{c_i+K_d} + \alpha\frac{K_d}{c_i+K_d}\right)$. The bracket term represents the probability of activation for a receptor experiencing c_i ligands. K_d is the equilibrium dissociation constant and α represents constitutive receptor activity, which we take to be small ($\alpha \ll 1$). In other words, the number of active receptors A_i given ligand count c_i is a Poisson random variable with mean μ_i. Equations 16 and 17 together specify the measurement kernel.

Input statistic

Next, we specify the input statistic $p(\boldsymbol{c})$ which will be determined by spatial distribution of ligands, thus differ between different classes of environment. Suppose a circular cell samples its environment by binding nearby ligands. The cell will encounter certain spatial profiles of ligands more often than others, and such statistics will likely depend on the type of environment the cell lives in. In this work, we studied three classes of environments: soil, tissue, and monotonic gradient. Closed form models do not exist for ligand profile statistics of natural environments. Therefore, we take an empirical approach, generating instances of each environment as the steady-state solution of a partial-differential equation (PDE) models and directly sample ligand profiles from them (see section on modeling chemical environment for details on all PDE models). For soil, we adopted mathematical models from Melke et al. (2010) and Raynaud and Nunan (2014), modeling diffusive ligands released from a group of soil bacteria whose spatial distribution agrees with the statistical properties of real soil colonies (Figures 1Ciii and 2A). For tissue, we adopted models from Milde et al. (2008) and Rejniak et al. (2013), where they modeled diffusive ligands released from a localized source, perturbed by *in vivo* processes such as interstitial fluid flow, non-uniform ECM binding and cell uptake, to represent an interstitial gradient (Figures 1Cii and 2B). We also considered a simple (monotonic) gradient (Figure 2C) which is an exponential fit to the simulated interstitial gradient (Figure 2B). Fitting ensures any difference between the two environments are due to differences in local structures, not global features such as gradient decay length or average concentration. For each environment, we obtain a ligand concentration field $c(x)$ as the steady-state solution of a PDE. Then, we tile it with a cell of fixed size and evaluate the concentration field along each cell membrane to obtain a set of ligand profiles denoted $\{\boldsymbol{c}\}$ (Figure 1Ci). Putting the empirical measure on the samples $\{\boldsymbol{c}\}$ approximates the true distribution of $\boldsymbol{C}$. It is important to note that although we modeled $p(\boldsymbol{c})$ and $p(\boldsymbol{a}|\boldsymbol{c})$ in these ways, the overall framework can accommodate any alternative choices of model.

For these choices of $p(\boldsymbol{c})$ and $p(\boldsymbol{a}|\boldsymbol{c})$, we aimed to study the functional relationship between ligand profiles $\{\boldsymbol{c}\}$ and their optimal receptor placements $\varphi^*(\boldsymbol{c})$. To this end, we optimized receptor profiles for each sampled profile $\boldsymbol{c}$ individually, reducing the general problem to a local formulation. Given ligand profile $\boldsymbol{c}$, the random vector $\widehat{\boldsymbol{c}}$ represents local fluctuations of $\boldsymbol{c}$ due to stochasticity of reaction-diffusion events. In the case of unimolecular reaction-diffusion processes, it can be shown that $\widehat{\boldsymbol{c}}$ is a Poisson random vector with mean equal to $\boldsymbol{c}$, solution of the PDE. Therefore, we can solve for $\varphi^*(\boldsymbol{c})$ locally by maximizing the mutual information between $\widehat{\boldsymbol{c}}$ and the resulting output $\widehat{\boldsymbol{a}}$:

$$\varphi^*(\boldsymbol{c}) = \underset{\substack{\boldsymbol{r}\geq 0\\ \sum_i r_i = N}}{\operatorname{argmax}}\, I(\hat{\boldsymbol{c}}, \hat{\boldsymbol{a}}|\boldsymbol{r}), \tag{Equation 18}$$

where $p(\hat{\boldsymbol{a}}) = \sum_{\boldsymbol{c}} p(\hat{\boldsymbol{a}}|\hat{\boldsymbol{c}} = \boldsymbol{c})p(\hat{\boldsymbol{c}} = \boldsymbol{c})$ and N is the total receptor number. We assume $\boldsymbol{r}$ to be real-valued instead of integer-valued when solving (Equation 18), this is reasonable as long as N is not too small.

The main difference between the general formulation of Equation 15 and local formulation of Equation 18 is their dependence on the input statistic $p(\boldsymbol{c})$. In the general formulation, the strategy $\varphi^*_{p(\boldsymbol{c})}$ is explicitly parametrized by $p(\boldsymbol{c})$. In the local formulation, φ^* is independent of the choice of $p(\boldsymbol{c})$. However, differences in $p(\boldsymbol{c})$ between environments will still crucially affect the set of optimal receptor profiles that cells will actually adopt. This is because changing $p(\boldsymbol{c})$ changes the region of the domain of φ^* that is most relevant, thus changing the optimal receptors profiles that are actually used in different environments. For example, suppose environment A and B have input statistic p_A and p_B with non-overlapping support, meaning that any ligand profile observed in A is not observed in B, and vice versa. Although φ^* is the same between A and B, this function is being evaluated on entirely different ligand profiles in A compared to B, so that receptor profiles observed in the two environment will likely be very different, in ways dictated by differences between their input statistic p_A and p_B. As a result, the statistical structure over the space of ligand profiles plays an important role in determining which receptor placement is effective, even when the placements are computed locally for each ligand profile.

The constrained nonlinear optimization problem of Equation 18 was evaluated using the fmincon routine of Matlab 2021 (MATLAB Optimization Toolbox, 2021a). The Sequential Quadratic Programming algorithm was used to ensure accurate solutions that may exist near the boundary of the feasible region. Furthermore, the analytical gradient of the objective function, shown in Equation 37, was supplied to ensure faster convergence.

Bin number and mutual information

An important point to emphasize is that the choice of m (number of discrete membrane bins) sets a scale for all information values reported in the paper, because the mutual information ($I(\boldsymbol{C};\boldsymbol{A})$) is bounded by the entropy of its input which scales logarithmically with m. We derive such an upper bound on $I(\boldsymbol{C};\boldsymbol{A})$ by first considering the following general property of mutual information. For any pair of discrete random variables X and Y, taking values in $\mathcal{X}$ and $\mathcal{Y}$, respectively, their mutual information $I(X;Y)$ can be equivalently expressed as,

$$\begin{aligned} I(X;Y) &= \sum_{x\in\mathcal{X}, y\in\mathcal{Y}} p_{(X,Y)}(x,y)\log\frac{p_{(X,Y)}(x,y)}{p_X(x)p_Y(y)} \\ &= \sum_{x\in\mathcal{X}, y\in\mathcal{Y}} p_{(X,Y)}(x,y)\log p_{X|Y=y}(x) - \sum_{x\in\mathcal{X}, y\in\mathcal{Y}} p_{(X,Y)}(x,y)\log p_X(x) \\ &= -\sum_{y\in\mathcal{Y}} p_Y(y)\mathrm{H}(X|Y=y) - \sum_{y\in\mathcal{Y}} p_X(x)\log p_X(x) \\ &= H(X) - H(X|Y). \end{aligned} \tag{Equation 19}$$

Since X and Y are discrete random variables, $H(X|Y)$ must be non-negative, which implies,

$$I(X;Y) \leq H(X). \tag{Equation 20}$$

Furthermore, suppose $X = (X_1,\ldots,X_m)$ is a discrete, multivariate random variables, then we can bound its entropy $H(X)$ using the fact that the joint entropy of a set of variables is less than or equal to the sum of the individual entropies of the variables in the set:

$$\begin{aligned} H(X) &\leq \sum_{i=1}^{m} H(X_i) \\ &\leq m \max_i H(X_i). \end{aligned} \tag{Equation 21}$$

Since $\boldsymbol{C} = (C_1,\ldots,C_m)$ and $\boldsymbol{A} = (A_1,\ldots,A_m)$ are both discrete (multivariate) random variables, Equations 20 and 21 both apply and we immediately get the following bound on the mutual information $I(\boldsymbol{C};\boldsymbol{A})$:

$$I(\boldsymbol{C};\boldsymbol{A}) \leq m \max_i H(C_i), \tag{Equation 22}$$

where m is the number of membrane bins. To simplify Equation 22 further, we will need to consider a specific sensing environment. Let us consider a cell sensing an average of $\bar{c}$ molecules distributed uniformly across space. In this simple environment, the number of ligand molecules at each of the m membrane bin are identically represented by a Poisson random variable with mean $\bar{c}/m$:

$$C_i \sim \mathrm{Pois}(\bar{c}/m),\ i = 1,\ldots,m. \tag{Equation 23}$$

Since all components C_i are now identically distributed, Equation 22 reduces to:

$$I(\boldsymbol{C};\boldsymbol{A}) \leq mH(C_i), \tag{Equation 24}$$

where $C_i \sim \mathrm{Pois}(\bar{c}/m)$. The entropy of a Poisson random variable C_i with parameter λ takes on the form:

$$H(C_i) = \lambda[1 - \log(\lambda)] + e^{-\lambda} \sum_{k=0}^{\infty} \frac{\lambda^k \log(k!)}{k!}, \tag{Equation 25}$$

where $\lambda = \overline{c}/m$. Combining Equations 24 and 25 gives the bound:

$$\begin{aligned} I(\boldsymbol{C};\boldsymbol{A}) &\le mH(C_i) \\ &\le m\left(\frac{\overline{c}}{m}[1 - \log(\overline{c}/m)] + e^{-\overline{c}/m} \sum_{k=0}^{\infty} \frac{(\overline{c}/m)^k \log(k!)}{k!}\right) \\ &\le \overline{c}[1 - \log(\overline{c}/m)] + e^{-\overline{c}/m} \sum_{k=2}^{\infty} \frac{\overline{c}^k \log(k!)}{k! m^{k-1}} \\ &\le \overline{c}[1 - \log(\overline{c}/m)] + \frac{1}{m} \sum_{k=2}^{\infty} \frac{\overline{c}^k \log(k!)}{k!}, \end{aligned} \tag{Equation 26}$$

where the second term goes to zero as m goes to infinity since the infinite sum converges. For large m, therefore, we obtain an upper bound on the mutual information $I(\boldsymbol{C};\boldsymbol{A})$ that scales logarithmically with the number of membrane bins m,

$$I(\boldsymbol{C};\boldsymbol{A}) \le \overline{c}(1 - \log(\overline{c})) + \overline{c}\log(m). \tag{Equation 27}$$

Figure S1A shows this upper bound (red) for $\overline{c} = 1$. As further validation of Equation 27; Figure S1A shows that as we increase receptor number N, $I(\boldsymbol{C};\boldsymbol{A})$ converges toward the derived upper bound. Furthermore, the result that optimizing receptor placement is significantly more beneficial in natural environments compared to simple gradients holds for a wide range of membrane bin numbers, as shown in Figure S1B where the absolute information gain (η, Equation 8) is significantly larger in natural environments compared to simple gradients, for a wide range of m values.

Theoretical properties of Poisson channels

In information theory, the Poisson channel is a canonical model used to study communication of information by random discrete occurrences in time that obey Poisson statistics. We show that we can map our receptor activation model directly onto this canonical model. As a result, we make use of existing results from information theory regarding the Poisson channel to 1) show that the localized receptor placement strategy described in the main text holds across most "reasonable" biochemical models of receptor activation, and 2) provide intuition for how different factors such as ligand concentration can alter the optimal strategy.

Mapping receptor model to the canonical Poisson channel model

We begin by showing how a single membrane receptor channel can be mapped to the canonical scalar Poisson model. The same argument applies for mapping multiple parallel membrane receptor channels to the canonical vector Poisson model introduced in the next section.

Recall the receptor model of Equation 17 we used to represent the number of active receptors A for a given ligand level $\boldsymbol{c}$, which is motivated by empirical measurements of receptor activity,

$$p(A = a | C = c, r) = \frac{\mu^a}{a!} e^{-\mu}, \ \mu = r\left(\frac{c}{c + K_d} + \alpha \frac{K_d}{c + K_d}\right). \tag{Equation 28}$$

Although this model of receptor activation consists of many biochemical details, we can map it directly onto the canonical scalar Poisson model,

$$Y | X \sim \text{Pois}(\beta X) \tag{Equation 29}$$

where X is a scalar input, Y is a scalar output, and β$ is a scaling variable. Such a model defines a Poisson channel whose output is a Poisson random variable conditioned on the input X with its mean equal to βX, where X is an arbitrary input random variable. We map this channel model maps onto our model of receptor activation for a single membrane region, by defining X, β in the following way:

$$\begin{aligned} X &:= f(C) = \frac{C}{C + K_d} + \alpha \frac{K_d}{C + K_d}, \\ \beta &:= r, \end{aligned} \tag{Equation 30}$$

where X represents the probability of receptor activation, r denotes the number of receptors. From this set of definitions, it follows that $Y = A$ is the number of active receptors. Note that β from Equation 29 is a constant value, rather than a function like the placement strategy φ. Therefore, Equation 30 agrees with our local formulation of Equation 18, and matches the general formulation of Equation 15 if φ is a constant function. An important consequence of this mapping is that we can now study the quantity $I(X, Y)$ since,

$$\begin{aligned} I(X;Y) &= I(f(C);A) \\ &= I(C;A), \end{aligned} \tag{Equation 31}$$

where the second line follows from the fact that the mutual information is invariant to invertible transformations f. Since most physical models of receptor activity (f) are strictly increasing functions of ligand count, hence invertible, theoretical properties of $I(X,Y)$ which we discuss here directly applies to many receptor models beyond what is considered in this work, such as models with signal amplification and receptor cooperativity. Note that we are leaving the probability distribution $P(X)$ unspecified, which again makes many of the following results valid for many choices of f.

Relating properties of $I(X,Y)$ to receptor sensing

Having established the relationship $I(X;Y) = I(C;A)$, we now use the scalar Poisson model to illustrate how theoretical properties of the mutual information $I(X,Y)$ agrees with our intuition of ligand sensing via receptor binding. We specialize to the case where X is a non-negative random variable which is sufficient for our problem as X only takes values between 0 and 1. In this setting, Theorem 2 of Guo et al. (2008) gives the partial information gain for the scalar Poisson channel as,

$$\frac{d}{dr} I(X;Y) = E[X\log X - E[X|Y]\log E[X|Y]]. \quad \text{(Equation 32)}$$

An immediate consequence of Equation 32 is that the mutual information $I(X;Y)$ (hence $I(C;A)$) is strictly increasing in the scaling variable (receptor number), which follows from the fact that the right side of Equation 32 is non-negative due to Jensen's inequality since $x \log x$ is a convex function. The fact that $I(X,Y)$ is strictly increasing in r agrees with the intuition that increasing the number of receptors should increase the amount of information the cell can acquire about its external environment.

Observe that the right hand side of Equation 32 is exactly the minimum mean loss in estimating X based on Y under the loss function $L(x_1,x_2) = x_1\log(x_1/x_2) - x_1 + x_2$. Using this fact, one can show that $I(X;Y)$ is a concave function of r, which again agrees with the intuition that since the total amount of information available $H(X)$ is fixed, incremental gain in information acquisition must diminish as more receptors are added. Importantly, the fact that $I(X;Y)$ is an increasing, concave function of the scaling variable r holds across all models of receptor activation (Equation 30). In particularly, the concavity of $I(X;Y)$ is a general phenomena and not a result of saturation from ligand binding.

Mapping full membrane receptor model to vector Poisson channel model

We will now rewrite our local optimization problem of Equation 18 using the canonical vector Poisson channel model. By doing so, we will be able to use theoretical properties of the vector Poisson model to provide additional insight into the optimal solution, and expand the result beyond the specific receptor model used in the main text. By a similar argument as in the scalar Poisson case, the full membrane receptor model considered in our work (Equation 3) maps exactly onto the canonical vector Poisson channel model, defined as

$$\boldsymbol{Y}|\boldsymbol{X} \sim \prod_{i=1}^{m} P(Y_i|\boldsymbol{X}) = \prod_{i=1}^{m} \mathrm{Pois}\left(Y_i\middle|(\Phi\boldsymbol{X})_i\right) \quad \text{(Equation 33)}$$

where the random vector $\boldsymbol{X} = (X_1, X_2, \ldots, X_m)$ maps to the probability of receptor activation across the m discretized membrane regions, the random vector $\boldsymbol{Y} = (Y_1, Y_2, \ldots, Y_m)$ maps to the random vector of active receptors $\boldsymbol{A} = (A_1, A_2, \ldots, A_m)$, the channel matrix $\Phi \in \mathbb{R}_+^{m\times m}$ can map onto receptor placement $\boldsymbol{r} = (r_1, r_2, \ldots, r_m)$ such that $\Phi = \mathrm{diag}(\boldsymbol{r})$. This mapping represents the fact that receptors bind ligands locally and activate independently of other receptors. We introduce Φ for completeness, showing that this model can accomodate situations where there are crosstalks between channels, leading to non-zero terms in the off-diagonal. Since the equivalent of Equation 31 holds for the vector model, we can rewrite the optimization problem in Equation 18 as,

$$\boldsymbol{r}^* = \underset{\substack{\boldsymbol{r} \geq 0 \\ \sum_i r_i = N}}{\operatorname{argmax}} \, I(\boldsymbol{X},\boldsymbol{Y}|\boldsymbol{r}). \quad \text{(Equation 34)}$$

By working with Equation 34, we derive results that hold for many models of receptor activation, including all models where activity is a monotonic function of ligand level.

Reformulation of receptor optimization in terms of partial information gain

We reformulate Equation 34 in terms of the partial derivatives $\partial I(\boldsymbol{X};\boldsymbol{Y})/\partial r_i$, which provides additional insight into the optimal solution. According to the Karush-Kuhn-Tucker (KKT) conditions, the following must hold at the optimal solution $\boldsymbol{r}^*$ for $1 \leq i \leq m$,

$$\begin{aligned} &\frac{d}{dr_i} I(\boldsymbol{X};\boldsymbol{Y}|\boldsymbol{r}^*) = \lambda - \mu_i, \\ &\mu_i r_i^* = 0, \end{aligned} \quad \text{(Equation 35)}$$

where $\mu_i \geq 0$ and λ are the KKT multipliers. Another way to interpret the equations above is that for all channels where the optimal receptor number r_i^* is non-zero, their partial derivatives $\frac{d}{dr_i} I(\boldsymbol{X};\boldsymbol{Y})|_{\boldsymbol{r}^*}$ must be equal. Put another way, optimal solution occurs when incremental information gain is matched across channels. Since whenever the partial derivatives do not all agree, then one can always move receptors from the channel with a smaller partial derivative to one with higher partial derivative to achieve a higher mutual information.

Asymptotic of the gradient of mutual information at small N

We show that when total receptor number is low, the partial information gain depends only on the properties of $\boldsymbol{X}$, the probability of receptor activation. This result allows us to directly solve for the optimal solution at the low N regime. Theorem 1 of Wang et al. (2014)

gives the gradient of mutual information between input and output of the vector Poisson channel $I(\boldsymbol{X};\boldsymbol{Y})$, with respect to the matrix Φ as,

$$\nabla_{\Phi} I(\boldsymbol{X};\boldsymbol{Y})_{ij} = E\left[X_j \log(\Phi \boldsymbol{X})_i\right] - E\left[E[X_j|\boldsymbol{Y}]\log E\left[(\Phi \boldsymbol{X})_i|\boldsymbol{Y}\right]\right]. \quad \text{(Equation 36)}$$

Specializing to the setting where Φ is a diagonal matrix with $\mathrm{diag}(\Phi) = \boldsymbol{r}$, the derivative of mutual information with respect to receptor number at position i is,

$$\frac{d}{dr_i} I(\boldsymbol{X};\boldsymbol{Y}) = E[X_i \log X_i] - E[E[X_i|\boldsymbol{Y}]\log E[X_i|\boldsymbol{Y}]]. \quad \text{(Equation 37)}$$

This derivative can be interpreted as the information gain at the i-th channel per receptor added.

When total receptor number (N) is low, corresponding to all scaling variables ($\{r_i\}$) being small, we can express Equation 37 as a function of just the random variable $\boldsymbol{X}$. First, using Lemma 1 from Dytso et al. (2020), we have

$$\begin{aligned} r_i E[X_i|\boldsymbol{Y} = \boldsymbol{y}] &= (y_i + 1)\frac{p_{\boldsymbol{Y}}(\boldsymbol{y}+1_i)}{p_{\boldsymbol{Y}}(\boldsymbol{y})} \\ &= r_i \frac{E\left[(X_i)^{y_i+1} e^{-r_i X_i} \prod_{m \neq i} \frac{1}{y_m!}(X_m)^{y_m} e^{-r_m X_m}\right]}{E\left[\prod_m (X_m)^{y_m} e^{-r_m X_m}\right]}. \end{aligned} \quad \text{(Equation 38)}$$

Therefore, for $r_i > 0$, we have

$$E[X_i|\boldsymbol{Y} = \boldsymbol{y}] = \frac{E\left[(X_i)^{y_i+1} e^{-r_i X_i} \prod_{m \neq i} \frac{1}{y_m!}(X_m)^{y_m} e^{-r_m X_m}\right]}{E\left[\prod_m (X_m)^{y_m} e^{-r_m X_m}\right]}. \quad \text{(Equation 39)}$$

Now using monotone convergence theorem, we obtain

$$\lim_{r_1,\ldots,r_m \to 0^+} E[X_i|\mathbf{Y} = \mathbf{y}] = \frac{E\left[(X_i)^{y_i+1} \prod_{m \neq i} \frac{1}{y_m!}(X_m)^{y_m} e^{-r_m X_m}\right]}{E\left[\prod_m (X_m)^{y_m}\right]} \quad \text{(Equation 40)}$$

The above limit holds for any path, and also holds for all value of $\boldsymbol{y}$ including zero. Evaluating the above limit at $\boldsymbol{y} = 0$ we have

$$\lim_{r_1,\ldots,r_m \to 0^+} E[X_i|\boldsymbol{Y} = 0] = E[X_i]. \quad \text{(Equation 41)}$$

Applying this limit to Equation 37 gives the desired result:

$$\lim_{r_1,\ldots,r_m \to 0^+} \frac{\partial}{\partial r_i} I(\boldsymbol{X};\boldsymbol{Y}) = E[X_i \log X_i] - E[X_i]\log E[X_i], \quad \text{(Equation 42)}$$

which we denote as

$$\frac{\partial I_0}{\partial r_i} : = \lim_{r_1,\ldots,r_m \to 0^+} \frac{\partial}{\partial r_i} I(\boldsymbol{X};\boldsymbol{Y}). \quad \text{(Equation 43)}$$

In this limit, the partial derivatives are independent of receptor number. Intuitively, when receptor numbers are low, the effect of diminishing return that comes from having many receptors should be weak. Importantly, this result holds for arbitrary distribution $P(\boldsymbol{X})$, hence it holds for any environmental statistic and model of receptor activation. As we show in the next section, this fact allows us to solve for the optimal solution $\boldsymbol{r}^*$ exactly in the low N limit.

Factors affecting optimal receptor placement

Total receptor number

Optimal receptor placement can be strongly localized when receptors are limited in quantity. When receptor number is small, Equation 42 shows that the $\frac{d}{dr_i} I(\boldsymbol{X};\boldsymbol{Y})$ becomes independent of receptor number. This result implies that $I(\boldsymbol{X};\boldsymbol{Y})$ is maximized when all receptors are allocated to the channel with the largest partial derivative $\frac{d}{dr_i} I(\boldsymbol{X};\boldsymbol{Y})$, resulting in strong receptor localization. We can see this by first noting that in the limit of small N, Equation 42 and Taylor's theorem allows us to write the mutual information as a linear function of $\boldsymbol{r}$,

$$I(\boldsymbol{X};\boldsymbol{Y}) = \sum_{i=1}^{m} \frac{\partial I_0}{\partial r_i} r_i \quad \text{(Equation 44)}$$

Hence, our optimization problem becomes a linear program with the following form:

$$\begin{aligned} &\text{maximize} \quad \boldsymbol{a}^T \boldsymbol{r} \\ &\text{subject to} \quad \boldsymbol{1}^T \boldsymbol{r} = r_{\text{tot}}, \quad \boldsymbol{r} \geq 0, \end{aligned} \quad \text{(Equation 45)}$$

where $a_i = \partial I_0 / \partial r_i$. Suppose the a_i's are sorted in increasing order (with corresponding r_i's rearranged as well),

$$a_1 \leq a_2 \leq \cdots < a_k = \cdots = a_{m-1} = a_m \quad \text{(Equation 46)}$$

Denote $a_{\max} := a_m$, we have

$$\boldsymbol{a}^T \boldsymbol{r} \leq a_{\max}\left(\mathbf{1}^T \boldsymbol{r}\right) = a_{\max} r_{\text{tot}} \quad \text{(Equation 47)}$$

for all feasible $\boldsymbol{r}$, with equality if and only if

$$r_k + \cdots + r_m = r_{\text{tot}}. \quad \text{(Equation 48)}$$

The optimal solution is then to allocate all receptors among the channels with maximal partial information gain $\partial I_0 / \partial r_i$, in any manner. This result is quite intuitive. If the channel information gains are fixed, we allocate all receptors to the channel with the highest gain. Since Equation 42 is valid for all non-negative random variable X, this result holds for arbitrary environmental statistics. Furthermore, since $\partial I_0 / \partial r_i = a_i \geq 0$ due to Jensen's inequality, the optimal solution remains unchanged if we replace the equality constraint by an inequality $\mathbf{1}^T \boldsymbol{r} \leq N$. Again, since we allow $P(\boldsymbol{X})$ to be arbitrary, this optimal solution holds for any environmental statistic and model of receptor activation. Figure S2 illustrates this result by optimizing across two Poisson channels for different number of receptors (N).

In line with the KKT condition of Equation 35; Figure S2 shows the optimal receptor distribution across the two channels (dotted lines) occurs precisely where their partial derivatives (solid lines) are equal. Even though channel 2 (orange) experience an average ligand concentration that is only 5% higher than channel 1, the optimal solution allocates nearly all receptors (98%) to channel 2 when N is small. As N increases, this asymmetry of the optimal solution reduces significantly, resulting in a 5% difference in receptor number between the two channels when $N = 200$. In agreement with results we derived, strong receptor localization occurs when N is small due to the fact that $\frac{d}{dr_i} I(X;Y)$ becomes nearly independent of receptor number (note the difference in y-range across the three plots in Figure S2).

Absolute ligand concentration and dynamic range

In addition to receptor number, environmental factors can strongly influence receptor placement. Intuitively, one would expect the larger the difference between two channels' input ligand concentration, the larger the asymmetry should be in their receptor allocation. Figure S3A confirms this intuition, showing that as the relative difference in average ligand concentration sensed between two channels increase, receptor distribution between the two channels becomes more asymmetric. Figure S3A also suggests two additional features of the optimal strategy that are less intuitive,

1. As ligand concentration increases, optimal strategy switches from allocating more to allocating less receptors to region of higher ligand concentration
2. When ligand concentration are either high or low, optimal receptor placement can become highly localized, concentrating most receptors to a few channels

The first feature can be seen by observing the fact that as $E[C_1]$ increases in Figure S3A, the optimal receptor distribution r_1^* / N (gray to black) changes from being below 0.5 to above 0.5, even though $E[C_2] > E[C_1]$ for all cases plotted. The second case can be seen by observing the slope of the graphs. As $E[C_1]$ becomes either high (black) or low (gray), the optimal receptor distribution becomes more sensitive to $(E[C_2] - E[C_1])/E[C_1]$, the relative difference in average input level. For a minor difference in concentration of $< 5\%$, nearly all receptors become allocated to one of the two channels.

Both of these observations are indeed general features of the optimal strategy and we can explain both using $\partial I_0 / \partial r_i$ defined in Equation 42. We can gain further intuition of both features from the shape of the binary entropy function (Figure S3C).

1. Figure S3B shows that when $E[X_1]$ is low, $\partial I_0 / \partial r_1$ is an increasing function in $E[X_1]$, suggesting that more receptors should be allocated to channels with higher probability of receptor activation (i.e. ligand concentration). However, this monotonicity switches as $E[X_1]$ increases, with $\partial I_0 / \partial r_1$ becoming a decreasing function in $E[X_1]$. The point at which monotonicity of $\partial I_0 / \partial r_1$ switches (dashed black line) matches precisely with when the optimal strategy switches from allocating more receptors to region of higher probability of receptor activation to region of lower probability, as shown by the solid black curve passing the dashed red line. Thus feature #1 can be fully explained by the gradient of mutual information. This switch in strategy is intuitive when we consider the binary entropy function. Recall that X_i maps to the probability of receptor activation in the i-th channel, so it shares a similar interpretation as the success probability p of the binary entropy function. The entropy function $H(p)$ is maximized when the success probability (analogously receptor activation) is neither high nor low (Figure S3C). Thus it can be less useful to place more receptors at regions of higher ligand concentration, since those receptors will simply stay activated, being uninformative of the input.
2. Figure S3B shows that the slope of $\partial I_0 / \partial r_1$ is maximized when $E[X_1]$ is either low or high. The larger the difference in the partial derivatives between two channels, the more receptors will need to be allocated before their partial derivative agree, a necessary condition for achieving optimality according to Equation 35. Therefore, a small relative difference in input concentration between channels can lead to large difference in information gain per receptor, when absolute ligand concentration is either high or low (relative to K_d), leading to strong localization of receptors. This behavior can also be explained using

the binary entropy function, specifically the fact that the rate of change in entropy is maximized at low and high success probability (Figure S3C). Analogously, placing receptors in regions where likelihood of activation is 0 or 1 is useless from an information perspective (zero entropy/uncertainty in output), so all receptors should be allocated to a region with non-zero entropy, no matter how small the difference in likelihood of activation (thus ligand concentration) is.

Chemical microenvironment models

Soil chemical microenvironment

In soil, free-living unicellular eukaryotes can sense and respond to signaling ligands secreted by soil bacteria. We follow mathematical models described in (Raynaud and Nunan, 2014) and (Melke et al., 2010), modeling the spatial distribution of ligands in two steps: 1) model the spatial distribution of bacteria in soil, and 2) model each bacteria as an independent point sources of ligands.

We follow the procedure outlined Raynaud and Nunan (2014), which allows us to generate realistic bacterial distributions found in soil. This procedure involves sampling from a spatial statistical model, based on Log Gaussian Cox Processes (LGCP) fitted to image data of observed bacterial distribution in soil. In a LGCP, the observed number of bacteria per unit area is modeled as a Poisson process in which the rate parameter is treated as being the exponential of a Gaussian process. Specifically, we consider Gaussian processes with an exponential covariance function,

$$C(r) = \sigma^2_{\text{bacteria}} e^{-r/\beta}, \qquad \text{(Equation 49)}$$

so the Gaussian process (and the LGCP) is fully determined by three parameters, its mean (μ), variance ($\sigma^2_{\text{bacteria}}$), and scale ($\beta$). In the limit as $\sigma^2_{\text{bacteria}} \rightarrow 0$, we obtain a homogeneous Poisson process. The average intensity of a LGCP (number of bacteria per unit area) is given by:

$$\lambda = e^{\mu + \sigma^2_{\text{bacteria}}/2} \qquad \text{(Equation 50)}$$

We used parameters reported in Raynaud and Nunan (2014), with $\mu = -7.52$, $\sigma^2_{\text{bacteria}} = 1.9$, and $\beta = 25$, to simulate a bacterial density of approximately 10^9cells/g on a 1000 × 3000μm^2 rectangular domain (containing approx. 4000 cells). These are the default parameters unless otherwise stated in the main text. We used RStudio v1.3 (RStudio Team, 2015) with packages *spatstat* (Baddeley et al., 2015) and *RandomFields* (Schlather et al., 2020) to generate all bacteria distributions.

Given a spatial distribution of bacteria, we model the distribution of secreted molecules using standard reaction-diffusion models (Melke et al., 2010). Specifically, such models treat each bacteria as a static, independent sources, producing ligands with rate α that diffuse (D) and degrade (γ). The resulting ligand concentration field is then the solution of the following partial-differential equation (PDE):

$$\frac{\partial c(x,t)}{\partial t} = \alpha|_{\text{bacteria}} + D\Delta c - \gamma c, \qquad \text{(Equation 51)}$$

Rather than approximating each parameter of Equation 51, we model the ligand distribution produced by a bacteria using a 2D Gaussian density profile, and directly fit the Gaussian profile to empirical measurements. The concentration c at a given position x in the domain is then the sum over all such Gaussian profiles evaluated at x, which can be expressed mathematically as

$$c(x) = \sum_{q \in \mathcal{U}} \frac{C}{\sqrt{2\pi s^2}} \exp\left\{-\frac{\left\|x - q\right\|^2}{2s^2}\right\} \qquad \text{(Equation 52)}$$

where $\mathcal{U}$ represents the set of bacterial positions generated using the LGCP model. C represents the total concentration of each Gaussian profile, and s determines the width of the profile, both of which are assumed to be uniform across all bacteria. We extract both parameters based on a geostatistical block kriging analysis of the spatial distribution of AHL in soil (C chosen such that mean concentration (across the entire spatial domain) is approximately 0.6 nM, $s = 9\mu$m) (Burton et al., 2005; Gantner et al., 2006; Sheng et al., 2017; Wang and Leadbetter, 2005).

Tissue chemical microenvironment

We follow mathematical models of ligand distribution in tissue outlined in Rejniak et al. (2013) and Milde et al. (2008), simulating a tissue environment using a PDE model that incorporates four transport mechanisms: (1) free diffusion, (2) ECM binding, (3) fluid advection, (4) cellular uptake. The spatial domain is a rectangle of size 300μm × 900μm. We model ligands being supplied through fluid flows from the left boundary of the domain, and penetrate the interstitial space between immobilized cells. Soluble ligands are then transported by diffusion and fluid flow, and become immobilized upon binding to an extracellular matrix (ECM) made up of networks of interconnected fibers containing ligand binding sites. We explicitly represent both ECM-bound (c_b) and soluble forms of the ligand (c_s), so that the total ligand concentration $c(x,t)$ at position x and time t is equal to,

$$c(x,t) = c_s(x,t) + c_b(x,t). \qquad \text{(Equation 53)}$$

Mathematically, we can describe the dynamics of the soluble fraction $c_s(x,t)$ as follows:

$$\frac{\partial c_s}{\partial t} = \kappa|_{\text{boundary}} - u(x,t) \cdot \nabla c_s + D\Delta c_s - \beta_c c_s|_{\text{cells}} - k_{\text{ECM}}(e(x) - c_b)c_s - \gamma_s c_s. \qquad \text{(Equation 54)}$$

1. The first term, κ, represents production/release of molecule at the left boundary.
2. The second term represents fluid transport, where $u(x,t)$ is the velocity field of the interstitial fluid with input flow speed u^{in} at the left boundary. We impose zero-velocity condition on the top and bottom boundary.
3. The third term represents diffusion with D as the ligand diffusion coefficient.
4. The fourth term represents cellular uptake with rate β_c, a process that only occurs near immobilized cells distributed across the domain.
5. The 5th term represents ECM binding. The concentration of ECM binding site $e(x)$ at position x is generated using a minimal model of ECM protein distribution (see paragraph on "Generating ECM fiber network"). Binding occur with rate proportional to $e(x) - c_b(x,t)$, the level of available ECM binding site. Since the on-rate of ECM binding is much larger than the off-rate, we assume the off-rate to be zero.
6. The last term represents enzymatic degradation of ligand.

The dynamics of ECM-bound fraction $c_b(x,t)$ is much simpler, involving a term corresponding to ECM binding, a degradation term due to enzymatic decay.

$$\frac{\partial c_b}{\partial t} = k_{\text{ECM}}(e(x) - c_b)c_s - \gamma_b c_b. \qquad \text{(Equation 55)}$$

To generate a ligand concentration field c, we take κ to be non-zero for a brief period of time, representing a bolus of ligand released. Then, we simulate the combined dynamics of bound and soluble fractions for sufficiently long until the ligand distribution $c(x,t)$ is relatively stable. In practice, we observe that $c \approx c_b$ after a sufficiently long period of time, since the soluble fraction quickly become insignificant due to fluid flow. The resulting concentration field represents an interstitial gradient. The average concentration is set by setting the release rate κ such that the concentration of the soluble fraction c_s matches measured chemokine concentration found in interstitial fluids (1pM-10 pM) (Clark et al., 2015; Wang et al., 2008).

To generate a distribution of ECM binding sites $e(x)$ (Equation 55), we use a minimal computation model of fiber network (Harjanto and Zaman, 2013; Lee et al., 2014; Schlüter et al., 2012). The model generates ECM fibers represented by line segments, which could represent fibronectin, collagen, laminin, or other fibrous matrix components. To position each fiber, one end of each segment is randomly positioned following a uniform distribution within the domain. The other end's position is determined by picking an angle, uniformly from $[0, 2\pi)$, and length sampled from a normal distribution with mean 75μm and standard deviation of 5μm (as measured for collagen by Friedl et al., 1997). In total, 4050 fibers were placed in the domain. For the PDE simulation, the generated network is discretized by counting the number of fibrous proteins around each node in the simulation lattice. The density of fiber within each node is then converted to a concentration value representing the level of ECM binding sites, resulting in an average concentration of ECM binding site of 520nM.

Simple chemical gradient

One of the simplest model of chemical gradient can be described by the following PDE,

$$\frac{\partial c(x,t)}{\partial t} = \alpha\delta(x_0) + D\Delta c - \gamma c, \qquad \text{(Equation 56)}$$

where ligands are produced at rate α from a localized source at x_0, diffuses with diffusivity D and undergoes first order degradation with rate γ. The steady-state solution of Equation 56 is a single exponential gradient,

$$c(x) = C_0 \exp(-x/\lambda), \qquad \text{(Equation 57)}$$

where the ligand concentration $c(x)$ only depends on distance x from the source, the concentration at the source boundary $C_0 = \alpha/(2\sqrt{D/\gamma})$ and the decay length $\lambda = \sqrt{D/\gamma}$. By taking the source location x_0 to be the entire left boundary of the spatial domain, the stimulated interstitial gradient is well-described by the exponential model. Specifically, by first averaging the interstitial gradient (along the axis parallel to the ligand source) and fitting the resulting 1-D profile to Equation 57 using Matlab's fit function, we obtain an excellent fit with correlation coefficient $R^2 = 0.98$. This fitted exponential profile is the simple, monotonic gradient used in the paper.

Dynamic protocol for receptor rearrangement

In a dynamically changing environment, receptor should redistribute in an efficient manner in order to maximize information acquisition. We extended our optimization problem of Equation 18 to incorporate a "cost" for changing receptor location. For a cell sensing a sequence of ligand profiles $\{\boldsymbol{c}_t\}_{t=1}^{T}$ over time, the optimal receptor placement $\boldsymbol{r}_t^*$ for $\boldsymbol{c}_t$ now depends additionally on $\boldsymbol{r}_{t-1}^*$, the receptor placement for the previous ligand profile,

$$\boldsymbol{r}_t^* = \underset{\substack{\boldsymbol{r} \geq 0 \\ \sum_i r_i = N}}{\operatorname{argmax}} \, I(\widehat{\boldsymbol{c}}_t; \widehat{\boldsymbol{a}} | \boldsymbol{r}) - \gamma W_1\left(\boldsymbol{r}_{t-1}^*, \boldsymbol{r}\right). \qquad \text{(Equation 58)}$$

Here, we model the cost for redistributing receptors using the Wasserstein-1 (W_1) distance. For completeness, we first introduce the formal definition of the W_1 distance before returning to a much simpler form that applies to our problem. Let $X \sim P$ and $Y \sim Q$ represent two random variables defined over $M \subset \mathbb{R}^d$. Further, let $\mathcal{J}(P,Q)$ denote all joint distributions J for (X,Y) that have marginal P and Q. The W_1 distance between P and Q is:

$$W_1(P,Q) = \inf_{J \in \mathcal{J}(P,Q)} \int_{M \times M} ||x - y||_1 dJ(x,y). \qquad \text{(Equation 59)}$$

One way to understand the above definition is to consider different ways of transporting a distribution of mass $P(x)$ to a different distribution $Q(x)$. Given some cost function associated with each unit of mass transported, the W_1 distance is the minimum transport cost achievable. In this way, the W_1 distance assumes that the transformation from P to Q occurs in an optimal manner. Note that this distance function is non-negative and symmetric, and does not require P and Q to be probability distributions, it applies whenever the total mass is preserved between P and Q.

Although Equation 59 is difficult to compute in general, it has a closed form for the special case of $d = 1$ which is the case we are considering. Instead of using the canonical form of the W_1 distance in 1-D, we need to use a generalized form that applies to distributions on a circle (Rabin et al., 2011). For two receptor distributions on the 1-D surface of a 2-D cell, represented as non-negative vectors $\boldsymbol{a}$ and $\boldsymbol{b}$ of length m, the W_1 distance takes on the form,

$$W_1(\boldsymbol{a},\boldsymbol{b}) = \sum_{i=1}^{m} \left| \varphi_i - \mu \right|, \qquad \text{(Equation 60)}$$

where $\varphi_i = \sum_{j=1}^{i} \left(\frac{a_j}{||a||_1} - \frac{b_j}{||b||_1} \right)$ and μ is the median of the set of values $\{\varphi_i, 1 \le i \le m\}$. We derive the gradient of equation 60 as:

$$\frac{\partial}{\partial a_k} W_1(\boldsymbol{a},\boldsymbol{b}) = \sum_{i=1}^{m} \operatorname{sgn}(\varphi_i - \mu) \sum_{j=1}^{i} \left(\delta_{jk} - \frac{a_j}{||a||_1} \right). \qquad \text{(Equation 61)}$$

We perform optimization with this gradient using the fmincon function (with sqp algorithm) in Matlab.

Numerical simulation of receptor feedback scheme

In our feedback scheme, receptor $r(x,t)$ is modeled by considering three redistribution mechanisms: (1) lateral diffusion of r along the plasma membrane ($D\nabla^2_{\text{memb}} r$), (2) endocytosis of r along the plasma membrane ($k_{\text{off}}\, r$), (3) incorporation of cytoplasmic pool of receptors, R_{cyto}, to the membrane at rate proportional to local receptor activity (hAR_{cyto}). $A(x,t)$ is a random variable that denotes receptor activity along the cell membrane, and is a function of local receptor number. Then, the equation describing the distribution of r across the cell membrane can be expressed mathematically as,

$$\frac{\partial r(x,t)}{\partial t} = D\nabla^2_{\text{memb}} r - k_{\text{off}}\, r + hAR_{\text{cyto}}, \qquad \text{(Equation 62)}$$

where the total number of receptors $r_{\text{tot}} = \int_{\text{memb}} r + R_{\text{cyto}}$ is fixed. We simulate receptor distribution by treating the cell membrane as a 1D space and the cytosol as a single, homogeneous compartment. This simplification allows us to simulate our PDE using the Crank-Nicolson method in one spatial dimension. Given space and time units Δx and Δt, respectively, the Crank-Nicolson method with $R_i^j := r(i\Delta x, j\Delta t)$ and $A_i^j := A(i\Delta x, j\Delta t)$ is given by the difference scheme

$$\frac{R_i^{j+1} - R_i^j}{\Delta t} = \frac{D}{2\Delta x^2}\left(R_{i+1}^j - 2R_i^j + R_{i-1}^j + R_{i+1}^{j+1} - 2R_i^{j+1} + R_{i-1}^{j+1}\right) - \frac{k_{\text{off}}}{2}\left(R_i^j + R_i^{j+1}\right) + \frac{hA_i^j}{2}\left(R_{\text{cyto}}^j + R_{\text{cyto}}^{j+1}\right) \qquad \text{(Equation 63)}$$

where, $i = 1,2,3,\ldots m$, representing m discrete membrane compartments and R_{cyto}^j represents the additional cytosol compartment. Since the membrane is represented by a circle, we have the following pair of conditions,

$$R_0^j = R_m^j,\ R_{m+1}^j = R_1^j. \qquad \text{(Equation 64)}$$

Lastly, total receptor number across all compartments is conserved:

$$\sum_{i=1}^{m} R_i^j + R_{\text{cyto}}^j = \sum_{i=1}^{m} R_i^{j+1} + R_{\text{cyto}}^{j+1}. \qquad \text{(Equation 65)}$$

Now, we can combined Equations 63, 64, and 65 and rewrite everything in vector form. First, let

$$\alpha := \frac{D}{2\Delta x^2},\ \beta := \frac{k_{\text{off}}}{2},\ \kappa_i^j := \frac{hA_i^j}{2},$$

and rewrite Equation 63 as,

$$\frac{R_i^{j+1}}{\Delta t} - \alpha\left(R_{i+1}^{j+1} - 2R_i^{j+1} + R_{i-1}^{j+1}\right) + \beta R_i^{j+1} - \kappa_i^{j+1} R_{\text{cyto}}^{j+1} = \frac{R_i^j}{\Delta t} + \alpha\left(R_{i+1}^j - 2R_i^j + R_{i-1}^j\right) - \beta R_i^j + \kappa_i^j R_{\text{cyto}}^j \qquad \text{(Equation 66)}$$

and define U^j to be the $(m+1)$-dimensional vector with components R_i^j for $i = 1,2,3,\ldots m$ and $U_{m+1}^j = R_{\text{cyto}}^j$. The difference scheme is given in the vector form

$$PU^{j+1} = QU^j. \qquad \text{(Equation 67)}$$

where,

$$P = \begin{bmatrix} \frac{1}{\Delta t}+2\alpha+\beta & -\alpha & 0 & \cdots & 0 & -\alpha & -\kappa_1^{j+1} \\ -\alpha & \frac{1}{\Delta t}+2\alpha+\beta & -\alpha & 0 & \cdots & 0 & -\kappa_2^{j+1} \\ 0 & \ddots & \ddots & \ddots & & & \vdots \\ \vdots & & \ddots & \ddots & \ddots & & \\ 0 & \cdots & 0 & -\alpha & \frac{1}{\Delta t}+2\alpha+\beta & -\alpha & -\kappa_{m-1}^{j+1} \\ -\alpha & 0 & \cdots & 0 & -\alpha & \frac{1}{\Delta t}+2\alpha+\beta & -\kappa_m^{j+1} \\ 1 & 1 & & \cdots & & 1 & 1 \end{bmatrix} \qquad \text{(Equation 68)}$$

$$Q = \begin{bmatrix} \frac{1}{\Delta t}-2\alpha-\beta & \alpha & 0 & \cdots & 0 & \alpha & \kappa_1^{j} \\ -\alpha & \frac{1}{\Delta t}-2\alpha-\beta & \alpha & 0 & \cdots & 0 & \kappa_2^{j} \\ 0 & \ddots & \ddots & \ddots & & & \vdots \\ \vdots & & \ddots & \ddots & \ddots & & \\ 0 & \cdots & 0 & \alpha & \frac{1}{\Delta t}-2\alpha-\beta & \alpha & \kappa_{m-1}^{j} \\ \alpha & 0 & \cdots & 0 & \alpha & \frac{1}{\Delta t}-2\alpha-\beta & \kappa_m^{j} \\ 1 & 1 & & \cdots & & 1 & 1 \end{bmatrix} \qquad \text{(Equation 69)}$$

Because A is invertible, the Crank-Nicolson scheme reduces to the iterative process

$$U^{j+1} = P^{-1}QU^j. \qquad \text{(Equation 70)}$$

The entire evolution of r can be solved where at each time step, we update receptor activity A_i^j across all membrane position i according to the random process described by Equations 16 and 17, followed by solving Equation 70 for U^{j+1}.

We set the value of the feedback constant h using empirical measurements from Marco et al. (2007). In Figure 3M of Marco et al., the authors report a quartile box plot showing estimated values for a parameter they call h (which we will refer to as $\overline{h}$), with a mean estimate of around $1.6 \times 10^{-3}s^{-1}$. Note $\overline{h}$ is equivalent in meaning as our hA_i. However, since hA_i will be different across different membrane bins and across time, we simulate the feedback scheme for a cell in a given environment and set the value of h such that the mean rate $\langle hA_i \rangle$ (averaged across membrane and time) is approximately equal to the mean estimate of $1.6\times10^{-3}s^{-1}$ reported by Marco et al. The value $\overline{h}$ reported by Marco et al., corresponds specifically to the transport rate of the Cdc42 to the membrane. The parameter value was obtained by analyzing fluorescence recovery of GFP-Cdc42 in membrane regions bleached with a laser pulse. Although the measured value corresponds to Cdc42, it has been used to model the effective exocytosis rate for receptors shown to undergo activity-dependent localization, showing good agreement with empirical data (Hegemann et al., 2015). Similar values around $10^{-3}s^{-1}$- $2\times10^{-3}s^{-1}$ have been measured for the recycling rate of a wide range of GPCRs (Lauffenburger and Linderman, 1993; Koenig and Edwardson, 1994, 1996; Pippig et al., 1995).

Simulation of cell navigation

Chemotaxis algorithm

At $t = 0$, initialize a cell at position $p_0 \in \Omega \subset \mathbb{R}^2$.

At each subsequent time step $t = t + \Delta t$ with the cell at position $p_t \in \Omega$:

1. Compute mean ligand profile $\boldsymbol{c} \in \mathbb{R}^m$ at the cell's current position.
2. Independently sample n ligand profiles $\{\boldsymbol{C}^{(i)}\}_{i=1}^{n}$ where each element C_j is distributed as a Poisson random variable with mean equal to c_j ($n = 30$ used in main text, refer to Figure S10 for other values of n).
3. For each ligand profile $\boldsymbol{C}^{(i)}$ sampled, sample a corresponding receptor activity profiles $\boldsymbol{A}^{(i)}$,

$$\boldsymbol{A}^{(i)} \middle| \boldsymbol{C}^{(i)} \sim \prod_{j=1}^{m} \mathrm{Pois}(\lambda_j), \text{ where } \lambda_j = r_j\left(\frac{C_j^{(i)}}{C_j^{(i)}+K_d} + \alpha\frac{K_d}{C_j^{(i)}+K_d}\right). \qquad \text{(Equation 71)}$$

4. Compute average receptor activity $\overline{\boldsymbol{A}} = \frac{1}{n}\sum_{i=1}^{n}\boldsymbol{A}^{(i)}$
5. Compute an estimator of gradient direction $\widehat{\theta}$ using one of three approaches
    - Optimal decoder + noise (Hu et al., 2010): $\widehat{\theta} = \arctan\left(\frac{\sin(\varphi)^T\overline{\boldsymbol{A}}}{\cos(\varphi)^T\overline{\boldsymbol{A}}}\right) + \mathcal{N}(0, 0.1)$, where $\varphi_i = 2\pi i/m, i = 1, \ldots, m$ corresponds to the angle where A_i is measured on the cell surface.
    - Random: $\widehat{\theta}$ is sampled uniformly from the set of m angles/directions $\{\varphi_i\}_{i=1}^{m}$
    - Maximal increase: $\widehat{\theta} = \varphi_{i^*}$ where

$$i^* = \underset{1\le i\le m}{\operatorname{argmax}} f(i) \quad \text{and} \quad f(i) = \begin{cases} \overline{A}_i - \overline{A}_{i+m/2} & i \le m/2 \\ \overline{A}_i - \overline{A}_{i-m/2} & i > m/2 \end{cases}$$

This decoder selects the direction of maximum change in receptor activity across the cell surface. In addition to the three decoders above, we consider the possibility of temporal averaging, where $\overline{\boldsymbol{A}}$ is a running mean over the past 5 minutes of receptor activity profiles (a total of $300\times30 = 9000$ sample profiles). This running average is decoded with the optimal decoder + noise as described above.

6. Set new cell position $p_{t+\Delta t} = p_t + s\Delta t[\cos(\widehat{\theta}), \sin(\widehat{\theta})]$, with speed $s = 2\mu m\ \text{min}^{-1}$, $\Delta t = 1\text{s}$.
7. Repeat from step 1.

Tissue gradient simulation for localization task

In addition to using the same tissue environment as the rest of the paper, we simulated additional tissue gradients using the same set of parameters but different (randomly generated) ECM fiber networks. This results in tissue gradients that have the same macroscopic features but different patterns of microscopic fluctuations.

Tissue gradient simulation for retention task

This task was motivated by the precision with which growth cones can retain themselves within specific regions of gradients of axon guidance cues. For this task, we used an ellipse-shaped cell with semi-major axis = 5μm, semi-minor axis = 2μm to mimic the shape of a navigating growth cone. In-vivo observations of axon guidance cue gradients show very short decay length (Xiao and Baier, 2007; Xiao et al., 2011), so we adjust several parameters to generate interstitial gradients with matching decay length. Table S3 contains new parameter values that differ from Table S1.

Extensions of framework to other strategies

We briefly illustrate an extension of our framework to study how cell shape can be tuned to improve cell sensing and navigation. Recall the generalized model of receptor activation from the discussion,

$$\mathbb{E}[A_i|c_i] = f(\boldsymbol{\theta}_i)\left(\frac{c_i}{c_i + K_d} + \alpha\frac{K_d}{c_i + K_d}\right), \tag{Equation 72}$$

where f is an unspecified function of an arbitrary set of variables $\boldsymbol{\theta}$, representing the "effective" number of receptors at position i.

Recent work has shown that given uniform membrane receptors sensing a uniform ligand field, membrane regions of higher curvature can exhibit higher receptor activity, due to higher local volume-to-surface ratio (Rangamani et al., 2013). Suppose we are interested in tuning membrane shape/curvature as a way to maximize information acquisition by cells. Assuming a constant, linear relationship between curvature at the i-th membrane position β_i and "effective" receptor number f, and that receptors are uniformly distributed, then we have

$$\mathbb{E}[A_i|c_i] = \alpha\frac{r_{\text{tot}}}{m}\beta_i\left(\frac{c_i}{c_i + K_d} + \alpha\frac{K_d}{c_i + K_d}\right), \tag{Equation 73}$$

where α is a proportionality constant and m is the number of membrane bins. This model is identical to our receptor model of Equation 28 up to a constant factor. Furthermore, if we assume a fixed total membrane area, the resulting optimization problem is nearly identical with Equation 18, where total membrane area now play a similar role as total receptor number, and β_i takes the place of r_i. Therefore, we expect general features of the optimal cell shape to match that of the optimal receptor placement. Namely, cells can maximize information acquisition by increasing membrane curvature at regions of high ligand concentration, by making narrow protrusions. One can derive a more accurate solution by considering a detailed model of the relationship between curvature and receptor activity outlined in Rangamani et al. (2013).

By extension, a strategy to dynamically form narrow membrane protrusions at regions of high ligand concentration, without explicitly tuning receptor positions, should in principle boost navigation efficiency in a manner similar to the receptor feedback scheme we proposed, as the two strategies have qualitatively similar effects on the spatial distribution of receptor activity. Recent works show that indeed a feedback circuit that produces dynamic, narrow membrane protrusions is crucial for neutrophil navigation. Cells that cannot form narrow protrusions can still move, but exhibit profoundly defective chemotaxis (Diz-Muñoz et al., 2016).